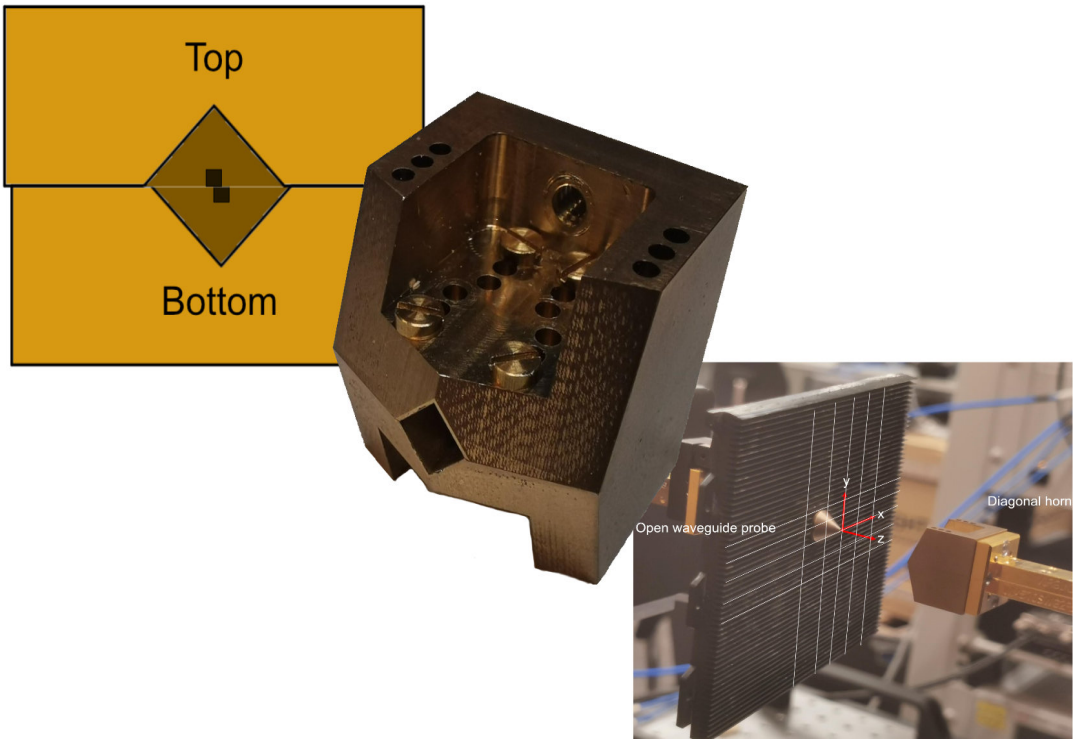

Sensitivity Analysis of Terahertz Horn Antennas

Effect of *E*-plane split-block misalignment

Master's thesis in Wireless, Photonics and Space Engineering

Andre George Koj

Department of Microtechnology and Nanoscience

CHALMERS UNIVERSITY OF TECHNOLOGY
Gothenburg, Sweden 2023
www.chalmers.se

Master's thesis 2023

Sensitivity Analysis of Terahertz Horn Antennas

Effect of E-plane split-block misalignment

Andre George Koj

CHALMERS
UNIVERSITY OF TECHNOLOGY

Department of Microtechnology and Nanoscience
Terahertz and Millimetre Wave Laboratory
Chalmers University of Technology
Gothenburg, Sweden 2023

Sensitivity Analysis of Terahertz Horn Antennas
Effect of E-plane split-block misalignment
Andre George Koj

Examiner and supervisor: Jan Stake, Department of Microtechnology and Nanoscience
Co-supervisor: Divya Jayasankar, Department of Microtechnology and Nanoscience

Master's Thesis 2023
Department of Microtechnology and Nanoscience
Terahertz and Millimetre Wave Laboratory
Chalmers University of Technology
SE-412 96 Gothenburg
Telephone +46317721000

Cover: a) Illustration of a diagonal horn's E-plane split-block misalignment, b) Picture of a high-precision machined brass diagonal horn, c) Picture showing a part of the near-field measurement setup.

Typeset in LaTeX
Printed by Chalmers Reproservice
Gothenburg, Sweden 2023

Sensitivity Analysis of Terahertz Horn Antennas
Effect of E-plane split-block misalignment
Andre George Koj
Department of Microtechnology and Nanoscience
Chalmers University of Technology

Abstract

Horn antennas are commonly integrated with waveguide components for terahertz applications. Typically, the antenna structure is milled with the waveguide feed in two metal halves, split along the E-plane, and clamped to form the horn antenna. However, misalignment between two split-blocks due to machining tolerances will degrade the coupling to a free-space fundamental Gaussian mode (Gaussicity). Especially at supra-terahertz frequencies (>3 THz), the tolerances can be a few per cent relative to the wavelength and radically degrade the optical coupling. This master thesis theoretically investigates the split-block misalignment's effect on a diagonal horn antenna, validated using a scaled experiment at 360 GHz. Moreover, the effect of misalignment is investigated for diagonal-spline and pyramidal horns to find a more robust alternative.

The analytical investigation found that an E-plane misalignment leads to a phase and amplitude shift between the TE_{10} and TE_{01} modes at the aperture of a diagonal horn, decreasing the Gaussicity. To verify the theoretical investigation, a diagonal horn is machined in split blocks with three different alignment cases and characterised using a WM-570 near-field measurement system. Finally, full-wave electromagnetic simulations of a diagonal, diagonal-spline and pyramidal horn at 360, 415 and 470 GHz are performed and compared for different alignment cases.

The measured radiation pattern of a diagonal horn agrees with the analytical and simulated results. A 2-dB decrease in Gaussicity is observed for a misalignment of 6% relative to the wavelength. Furthermore, based on simulated results, a diagonal-spline horn has a Gaussicity of 96% and deteriorates less with misalignment than a diagonal horn. In addition, a simple pyramidal horn, with a Gaussicity of 88%, is the least sensitive to misalignment due to the single-mode operation.
A diagonal horn is susceptible to alignment errors and, therefore, is concluded to be less suitable as an E-plane split horn for wavelengths where the alignment tolerance is significant. In contrast, the pyramidal or diagonal-spline horns are more robust against E-plane misalignment errors.

Keywords: Far-infrared, Gaussicity, horn antennas, near-field measurements, split-block, sub-millimetre wave components, terahertz technology

Acknowledgements

I would like to thank Prof. Jan Stake for his support and insightful advice during this project. His approach to research is very inspiring and is something I wish to carry with me moving forward. I would also like to thank my co-supervisor Divya Jayasankar for all the help she has provided me during this time. The dedication she has to her work is something I hope to emulate in my career.

I am also grateful to Dr Jeffrey Hesler for his advice on the measurement setup and the pyramidal horn. I would also like to thank Mr Mats Myremark for the high-precision machining.

This M.Sc thesis was carried out in the Gigahertz Center at Chalmers University of Technology in a project financed by VINNOVA, Chalmers University of Technology, Omnisys Instruments AB, Low Noise Factory, Wasa Millimeter Wave, the Research Institutes of Sweden (RISE), and Virginia Diodes, Inc. (VDI).

Andre George Koj, Gothenburg, June 2023

List of Acronyms

Below is the list of acronyms that have been used throughout this thesis listed in alphabetical order:

AUT	Antenna under test
CNC	Computer numerical control
EM	Electromagnetic
FEM	Finite element method
HPBW	Half-power beam width
HFSS	High-frequency structure simulator
NF/FF	Near-field to far-field
RF	Radio Frequency
PC	Personal computer
PEC	Perfect electric conductor
QCL	Quantum cascade laser
QO	Quasi-optical
TE	Transverse electric
TEM	Transverse electromagnetic
TM	Transverse magnetic
VNA	Vector network analyser

Nomenclature

Below is the nomenclature of indices, sets, parameters, and variables that have been used throughout this thesis.

Indices

m,n	Indices for Hermite-Gaussian modes
i,j	Indices for rectangular waveguide modes

Parameters

w	Beam radius
w_0	Beam waist
$\eta_{coupling}$	Coupling coefficient
D	Directivity/Largest aperture dimension
E_{ap}	Electric aperture field
ϵ_G	Gaussicity
R	Phase radius of the curvature
Φ_0	Phase shift
ϵ_G	polarisation factor

Variables

ϕ	Angle from the positive x-axis to the projection of the vector to the xy-plane
θ	Angle from the positive z-axis to the projection of the vector to the zy-plane
Δy	Split-block misalignment

Contents

List of Figures

1

Introduction

The interest in developing technology for terahertz (THz) applications has been increasing over the last decades [1]. The THz region (300 GHz $< f <$ 10 THz) provides wide bandwidth, noninvasive sampling and covers the rotational lines of certain molecules [2, 3]. These properties have made the region desirable for communication [4], biological sciences [5] and radio astronomy [6]. However, due to the high attenuation of THz signals in conventional waveguides, the signals are often propagated through free space as optical beams. Optimally, the optical power in the beams is contained in one mode, commonly the fundamental Gaussian mode [7]. Therefore, a Quasi-Optical (QO) system requires antennas with a high coupling to a fundamental Gaussian mode to reduce signal loss between free space and components.

The planar lens antenna is a common radiation coupling device for supra-THz (>3 THz) components, which provides high directivity and Gaussicity [8]. Using a thick silicon substrate on a hyper-hemispherical lens makes the mounting process simple. The drawback of such an antenna is the difficulty in matching the Gaussian beam parameters to external optical components [9]. It is, therefore, important to have feedhorns that can couple the Gaussian beam from the power source, maximise the coupling to detectors and have low cross-polarisation at supra-THz frequencies. A corrugated horn fulfils such requirements since it radiates an almost perfect Gaussian beam (98% Gaussicity) [10], but is impractical to produce above frequencies around 1.5 THz due to tolerance limits [11]. Other widely used alternatives like the Picket-Potter [12] and standard conical horn [13] require a circular to rectangular waveguide transition. Therefore, antennas with simpler designs and a direct rectangular transition, like diagonal horn antennas, are preferred. Another advantage is their convenience to the split-block technique, commonly used for metallic waveguide-led mixers at sub-millimetre wavelengths [14]. By machining a block in two pieces and milling the waveguide cross-section channel in both halves, this technique avoids losses in the TE_{10} mode since the split does not affect the surface currents of the mode [14]. While there are alternatives to Computer Numerical Control (CNC) milling, such as silicon micromachining, the chip-chip alignment has to be done post-fabrication, which leads to a misalignment similar to CNC milling [15, 16].

Table 1.1: Table of the Gaussicity of various feed antennas [7].

Feed type	w/a	**Gaussicity (%)**
Corrugated horn	0.64	98
Pyramidal horn	0.7	88
Conical horn	0.88	89
Diagonal horn	0.43	84
Lens + planar antenna	-	89

Horn antennas produced with the split-block technique have to be joined with the other half after machining, which is usually done with the help of alignment pins. However, The alignment tolerance of the two blocks can be as high as a few micrometres, which can be considered a non-factor for gigahertz frequencies. However, this misalignment can lead to disruptions in the propagation of the signals at supra-THz frequencies where waveguide dimensions are also in the micrometres. Dunning *et al.* [17] have noted the misalignment effect in orthomode transducers and how it increases unwanted properties. In 2016 [18] and 2018 [19], Hammar *et al.* observed that a lateral split-block misalignment leads to additional cross-polarisation. Jayasankar *et al.* [20] have noted this effect in mixer design and concluded that block fabrication immunity on the RF side could improve the performance of the harmonic mixer. However, it is difficult to ensure a misalignment below 2 μm due to errors in the fabrication and alignment processes. Hence, it is desirable to study the split-block misalignment in diagonal horns; and possibly provide an alternative horn used in future supra-THz designs.

This thesis studies the effect of split-block misalignment on three types of horn antennas to demonstrate their robustness as E-plane split horns at supra-THz frequencies. A theoretical and experimental evaluation of the misalignment on the diagonal horn at the WM-570 band (325-500 GHz) is presented, and a 3D-electromagnetic (EM) model was implemented using a Finite Element Method (FEM) solver (Ansys HFSS) to simulate the misalignment's effect on the three horns' performance. This thesis begins with an overview of antenna properties, horn antennas, Gaussian-Hermite analysis and antenna measurement theory. It is followed by Chapter 3 on the horn antennas and the misalignment study using theory and full wave-EM simulations. Chapter 3 also includes the setup procedure of the measurement system, its restrictions and advantages. It is followed by Chapter 4, which presents the results obtained from the simulations and the measurements. Finally, Chapter 5 concludes the thesis by showing the misalignment's effect on the horns' performance and which horn antenna is preferred at supra-THz frequencies.

2

Theory

This chapter starts with basic antenna concepts. Following that, Gaussian beam approximation theory is outlined. Moreover, The chapter lists the three types of horn antennas studied in this thesis and provides the theoretically expected Gaussian performance for the standard diagonal horn. Finally, the chapter concludes with the measurement theory used to obtain the far-field radiation pattern.

2.1 Antenna characteristics

Antennas, in general, are designed for a certain application, which is commonly quantified using their radiation pattern. The radiation pattern of an antenna represents the radiated energy's spatial distribution as a function of the receiver position. However, it is vital to highlight that, due to reciprocity, whether an antenna is transmitting or receiving, the radiation pattern characteristics are equal for both cases and so is the power flow. Reciprocity for antenna patterns is provided if the materials used for the antennas and the wave propagation media are linear and non-magnetic [21]. Therefore, in the following chapters, the models of the horn antennas are set as transmitters to simplify calculations.

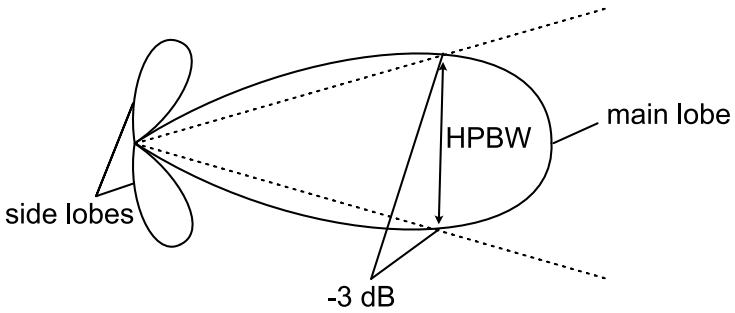

Figure 2.1: Illustration of the radiation pattern of a typical horn antenna.

The radiation pattern consists of the main lobes and a number of minor side lobes, which can be defined as portions of the radiation pattern that do not coincide with the main lobe. Typically, the main lobe is the direction of maximum radiation, while the side lobes lead to radiation in unwanted directions. It is, therefore, desirable to minimise the side lobes as much as possible.
Another important aspect of the radiation pattern is the Half-Power Beam Width

(HPBW), which is the angular separation between two points where the maximum power of the beam is halved. The HPBW is a decent indication of the resolution capability of an antenna to distinguish between two sources. If the two sources have an angular separation less than the HPBW, they would not be distinguished. The antenna designer has to optimise these properties to the desired application since there is a trade-off between beam width and side lobe levels, as the side lobe levels increase when the beam width decreases.

Directivity is another important characteristic of an antenna in a system. It is the ratio of radiation intensity at a certain direction compared to an isotropic antenna. If the radiation intensity U (power per unit angle) is known, the directivity D is given by:

$$D = \frac{U(\theta, \Phi)}{P_{tot}} = \frac{4\pi U(\theta, \Phi)}{\int\int_{\Omega} U \, d\Omega}. \tag{2.1.1}$$

The directivity is implied to be in the direction of maximum radiation unless a specific direction is given.

The radiation pattern is commonly expressed for a two-dimensional plane and the two most used planes are the E-plane (parallel with the electric field vector and propagation direction) and the H-plane (normal to the electric field vector and parallel to the propagation direction). Having the radiation pattern of an antenna in these two planes expresses many of the antenna's characteristics, making them a popular way to present an antenna's performance. There is also the lesser-used D-plane, which is an intermediate plane between the E-plane and the H-plane at a 45° angle, which can be of interest to study the symmetry of radiation patterns.

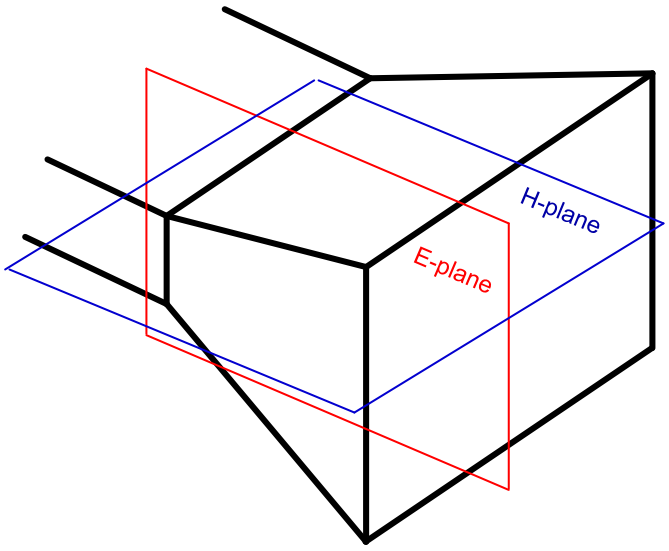

Figure 2.2: Illustration demonstrating the E and H-planes on a pyramidal horn.

2.2 Gaussian beam modes

Gaussian beams play a significant role in understanding quasi-optical systems [7]. In this section, relevant Gaussian beam formulas are derived from the paraxial wave equation. Higher-order modes are also covered in this section, which can be used to demonstrate the power coupling to different modes and, most significantly, to a fundamental Gaussian mode.

2.2.1 The paraxial wave equation

The case which is considered here is of a beam radiation that is largely collimated [22], which entails that it has a well-defined propagation direction but has a non-zero transverse variation (unlike a plane wave). It differs from a source in geometrical optics since it originates from a region of finite extent, rather than a point source. A single component Ψ, of an electromagnetic wave propagating in a uniform medium, satisfies the Helmholtz equation to

$$\nabla^2\Psi + k^2\Psi = 0, \tag{2.2.2}$$

where $k = \frac{2\pi}{\lambda}$. In Cartesian coordinates the Helmholtz equation for the electric field can be written as:

$$\frac{\partial^2 E}{\partial x^2} + \frac{\partial^2 E}{\partial y^2} + \frac{\partial^2 E}{\partial z^2} + k^2 E = 0. \tag{2.2.3}$$

For a beam propagating in the positive z-direction, any component of the E-field can be written as:

$$E(x, y, z) = u(x, y, z)e^{-jkz}, \tag{2.2.4}$$

where $u(x, y, z)$ is a slowly changing function which represents the non-planar part of the beam. If this is substituted in equation 2.2.3, it would result in the following:

$$\frac{\partial^2 u}{\partial x^2} + \frac{\partial^2 u}{\partial y^2} + \frac{\partial^2 u}{\partial z^2} - 2jk\frac{\partial u}{\partial z} = 0. \tag{2.2.5}$$

The third term $\frac{\partial^2 u}{\partial z^2}$ can be neglected since the change of the amplitude in the z-direction is assumed to be significantly smaller than the variation in the perpendicular directions. This demonstrates the low loss of the propagating beam, which is desirable at THz frequencies. Removing the third term results in what is called the paraxial wave equation,

$$\frac{\partial^2 u}{\partial x^2} + \frac{\partial^2 u}{\partial y^2} - 2jk\frac{\partial u}{\partial z} = 0. \tag{2.2.6}$$

The paraxial wave equation can be solved in Cartesian and cylindrical coordinate systems. A special case solution where the beam waist in x and y-axes is equal at the same value of z. In this case, the solution for a certain mn mode is:

$$\begin{aligned} E_{mn} = &\sqrt{\frac{1}{\pi w^2 2^{m+n-1} m! n!}} H_m\left(\frac{\sqrt{2}x}{w}\right) H_n\left(\frac{\sqrt{2}y}{w}\right) \\ &\cdot \exp\left[-\frac{(x^2+y^2)}{w^2} - jkz - \frac{j\pi(x^2+y^2)}{\lambda R} + j(m+n+1)\Phi_0\right], \end{aligned} \tag{2.2.7}$$

where R is the phase radius of the curvature, w is the beam radius and $\Phi_0 = \tan^{-1}\left(\frac{\lambda z}{\pi w_0^2}\right)$ is the phase shift. The beam radius is defined by the axial (orthogonal to propagating direction) distance where the amplitude of the field has dropped by a factor of $\frac{1}{e}$. The beam waist is the minimum value of the beam radius and occurs at a certain distance z depending on where the reference point is located. The beam waist is set by the dimensions of the aperture the beam is launched from, as seen in Figure 2.3. If the beam waist is known then the beam radius w at a certain distance z from the waist can be determined by:

$$w^2(z) = w_0^2 \left[1 + \left(\frac{z\lambda}{\pi w_0^2}\right)^2\right]. \tag{2.2.8}$$

The phase radius of curvature R describes the distance from a surface of the beam with equal phase to an assumed source that is generating spherical waves. At the beam waist, R can be seen as being infinite since the beam hasn't diverged and appears like a plane wave. Additionally, R will converge towards the distance z at large distances ($>> \frac{\pi w_0}{\lambda}$), which can be observed in the function,

$$R(z) = z \left[1 + \left(\frac{\pi w_0^2}{\lambda z}\right)^2\right]. \tag{2.2.9}$$

The phase shift term Φ describes the phase difference between a Gaussian mode and a plane wave. It is dependent on the propagation distance and the Hermite-Gaussian mode number. The Hermite-Gaussian phase term is given by:

$$\Phi_{mn} = (m + n + 1)\tan^{-1}\left(\frac{\pi w^2}{\lambda R}\right) = (m + n + 1)\tan^{-1}\left(\frac{\lambda z}{\pi w_0^2}\right). \tag{2.2.10}$$

The beam can be described by an infinite set of free-space modes for any value of w and R.

2.2.2 Gaussicity

The term Gaussicity was coined by Johansson [23] in 1995. It expresses the maximum achievable power coupling of the aperture field of a feed to a linearly polarised Gaussian beam. This parameter is relevant in a quasi-optical system where feeds are commonly coupled to a fundamental Gaussian mode. The Gaussicity can be expressed with the electric field $\mathbf{E}$ on the aperture surface A,

$$\epsilon_G = \frac{\left|\langle \mathbf{E}|\mathbf{g}\rangle\right|^2}{\langle \mathbf{E}|\mathbf{E}\rangle \langle \mathbf{g}|\mathbf{g}\rangle}, \tag{2.2.11}$$

where the coupling integral is defined as:

$$\langle \mathbf{f}|\mathbf{g}\rangle = \iint_A \mathbf{f} \cdot \mathbf{g}^* dA. \tag{2.2.12}$$

The Gaussian beam function is given by:

$$\mathbf{g}(r, \rho) = e^{-(\frac{r}{w})^2} \hat{a}_{copolar}, \tag{2.2.13}$$

where $\hat{a}_{copolar}$ is the co-polarisation unit vector.

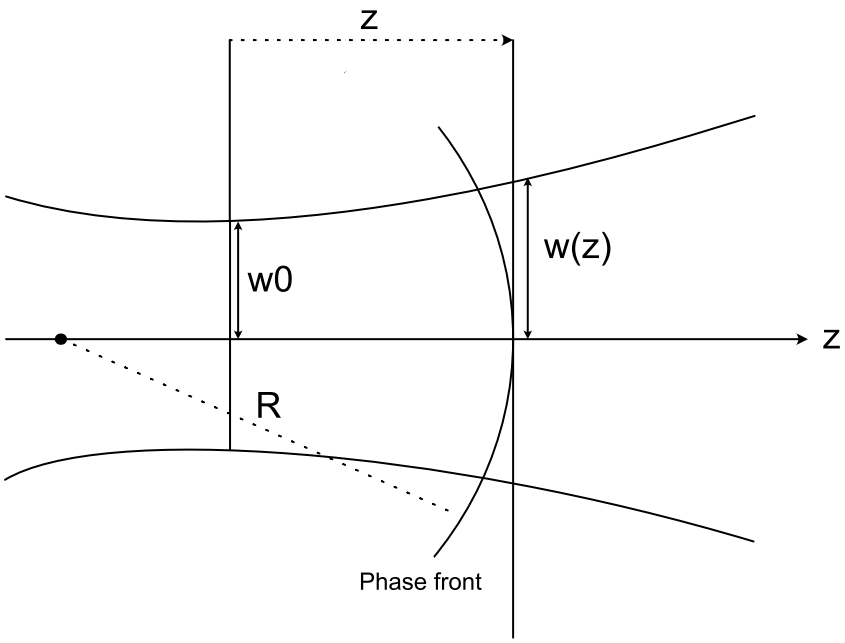

Figure 2.3: Illustration of a Gaussian beam contour.

2.3 Horn antennas

Waveguide technology at millimetre and sub-millimetre wavelengths is commonly implemented with metal blocks. The standard technique to form the blocks is the split-block technique. The block is machined in two halves and the waveguide is formed by milling a square cross-section channel in each half. The split is made along the centre of the broad walls of the waveguide in the a direction, which minimises the losses from the surface current discontinuity. The split-block structure requires high-quality fabrication by CNC milling and a precise assembly approach to obtain sufficiently satisfactory electrical and physical contact between the parts. When approaching THz frequencies, the assembly process becomes more crucial since the block misalignment, which is a non-factor for lower frequencies, starts to affect the performance.

2.3.1 Diagonal horn antenna

The diagonal horn antenna was introduced in 1962 by Love [24]. In 1992, Johansson presented a theoretical investigation of the horn as a sub-millimetre wave antenna [14]. The main reason why the diagonal horn is preferred at supra-THz frequencies is due to the geometrical form of the horn, which is relatively simple to mill using CNC milling. The diagonal horn has the following electric field distribution at the aperture:

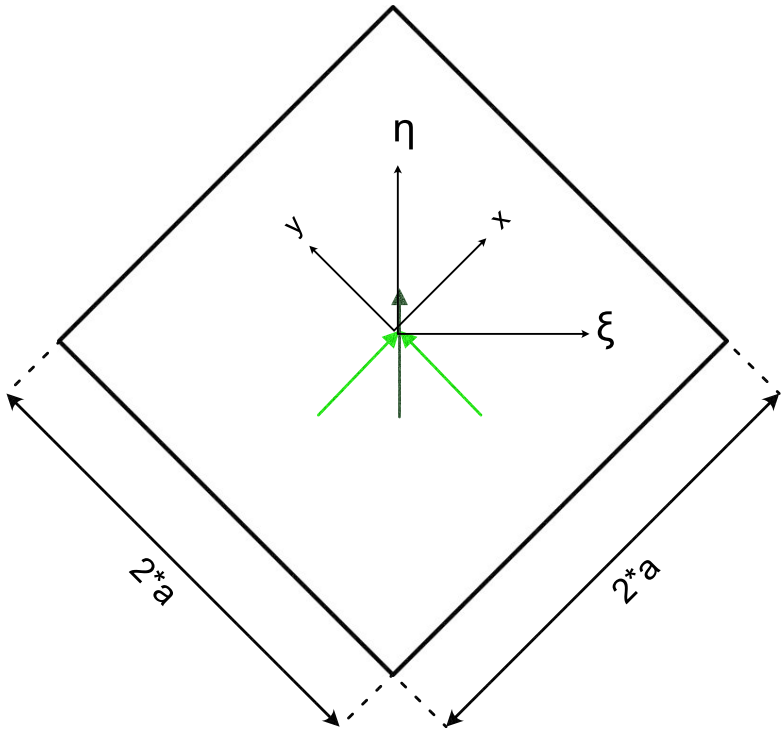

Figure 2.4: Aperture geometry of the diagonal horn with the TE_{10} and TE_{01} modes illustrated.

$$
\begin{aligned}
&E_{ap} = E_0 \left[\hat{x}\, cos\left(\frac{\pi y}{2a}\right) + \hat{y}\, cos\left(\frac{\pi x}{2a}\right) \right] e^{jk\delta} \\
&|x| \;<\; a,\; |y| \;<\; a \\
&k\delta = \frac{2\pi}{\lambda} \left[\frac{2a^2 - x^2 - y^2}{2L} \right].
\end{aligned}
\tag{2.3.14}
$$

The aperture field can be seen as a superposition of the TE_{10} and the TE_{01} modes, with equal power distributed between them. Love used a circular waveguide transition from TE_{10}, but the direct transition from a rectangular waveguide as shown by Johansson works well enough for most applications. This is due to the geometry of the diagonal horn, which can be seen in Figure 2.4. The diagonal horn has a flaring square waveguide rotated by 45°, making the two modes an equal angle apart from the TE_{10} electric field orientation. The co-polarisation (copolar) and cross-polarisation (crosspolar) components of the field can be expressed by introducing a coordinate system rotated by 45°, as the system in Figure 2.4. The corresponding

field components in the new coordinate system are written as:

$$\begin{aligned} E_\eta = \hat{\eta} \cdot \mathbf{E}_{ap} &= \frac{E_0}{\sqrt{2}} \left[cos\left(\frac{\pi(\eta-\xi)}{2\sqrt{2}a}\right) + cos\left(\frac{\pi(\eta+\xi)}{2\sqrt{2}a}\right)\right] e^{jk\delta} \\ &= \sqrt{2}E_0 cos\left(\frac{\pi\xi}{2\sqrt{2}a}\right) cos\left(\frac{\pi\eta}{2\sqrt{2}a}\right) e^{jk\delta} \\ &= \frac{E_0}{\sqrt{2}} \left[cos\left(\frac{\pi y}{2a}\right) + cos\left(\frac{\pi x}{2a}\right)\right] e^{jk\delta}, \end{aligned} \tag{2.3.15}$$

$$\begin{aligned} E_\xi = \hat{\xi} \cdot \mathbf{E}_{ap} &= \frac{E_0}{\sqrt{2}} \left[cos\left(\frac{\pi(\eta-\xi)}{2\sqrt{2}a}\right) - cos\left(\frac{\pi(\eta+\xi)}{2\sqrt{2}a}\right)\right] e^{jk\delta} \\ &= \sqrt{2}E_0 sin\left(\frac{\pi\xi}{2\sqrt{2}a}\right) sin\left(\frac{\pi\eta}{2\sqrt{2}a}\right) e^{jk\delta} \\ &= \frac{E_0}{\sqrt{2}} \left[cos\left(\frac{\pi y}{2a}\right) - cos\left(\frac{\pi x}{2a}\right)\right] e^{jk\delta}. \end{aligned} \tag{2.3.16}$$

Observing the aperture field distribution in the $\eta\xi$ coordinate system, it is clear that the copolar field (η-directed) is symmetric with respect to said coordinate system. The crosspolar aperture field (ξ-directed) is anti-symmetric and has a null at the boresight [25].

As mentioned in section 2.2, a Gaussian mode model is useful to study the radiation pattern of an aperture antenna. If the aperture field E_A is assumed to be able to contain the phase variation in a spherical phase factor, as in:

$$E_A(x,y) = E(x,y,z_A) = g(x,y) \exp\left[\frac{-jk[x^2+y^2]}{2R_A}\right], \tag{2.3.17}$$

then equation 2.2.7 is reduced to a more convenient form. The coefficients A_{mn} can be found using the orthogonality properties of Hermite polynomials in addition to algebraic adjustments,

$$A_{mn} = \frac{2}{\pi w_A^2} \iint_{-\infty}^{\infty} g(x,y) H_m\left[\frac{\sqrt{2}x}{w_A}\right] H_n\left[\frac{\sqrt{2}y}{w_A}\right] \, dx\, dy. \tag{2.3.18}$$

If the $g(x,y)$ function is real-valued, numerical complications due to phase variations can be avoided. The diagonal horn, which has no phase variation over the aperture except the spherical wave term is a good fit for the Gauss-Hermite analysis. Using the copolar and crosspolar parts given by equations 2.3.15 and 2.3.16, the $g(x,y)$ function is obtained for the diagonal horn. The mode fractional power content is given by:

$$\frac{P_{mn}}{P_{tot}} = \frac{\pi w_A^2}{2} \frac{|A_{mn}|^2}{\iint_{-\infty}^{\infty} |g(x,y)|^2 \, dx\, dy}, \tag{2.3.19}$$

which for a standard diagonal horn, will be the following:

$$\frac{P_{mn}^{co}}{P_{tot}} = \frac{\frac{64}{\pi}\frac{a^2}{w_A^2}\left|\int_0^1\int_0^{1-u} cos(\frac{\pi u}{2})cos(\frac{\pi v}{2})H_m\left[\frac{\sqrt{2}x}{w_A}\right]H_n\left[\frac{\sqrt{2}y}{w_A}\right]\,dv\,du\right|^2}{\int_{-1}^0\int_{-1-u}^{1+u}|cos(\frac{\pi u}{2})cos(\frac{\pi v}{2})|^2\,dv\,du + \int_0^1\int_{-1+u}^{1-u}|cos(\frac{\pi u}{2})cos(\frac{\pi v}{2})|^2\,dv\,du} \quad \text{even } m,\ n \tag{2.3.20}$$

$$\frac{P_{mn}^{xp}}{P_{tot}} = \frac{\frac{64}{\pi}\frac{a^2}{w_A^2}\left|\int_0^1\int_0^{1-u} sin(\frac{\pi u}{2})sin(\frac{\pi v}{2})H_m\left[\frac{\sqrt{2}x}{w_A}\right]H_n\left[\frac{\sqrt{2}y}{w_A}\right]\,dv\,du\right|^2}{\int_{-1}^0\int_{-1-u}^{1+u}|sin(\frac{\pi u}{2})sin(\frac{\pi v}{2})|^2\,dv\,du + \int_0^1\int_{-1+u}^{1-u}|sin(\frac{\pi u}{2})sin(\frac{\pi v}{2})|^2\,dv\,du} \quad \text{odd } m,\ n. \tag{2.3.21}$$

The choice of the $\frac{w_A}{a}$ ratio is arbitrary, but maximum coupling to the fundamental mode is usually desired. This choice will give the highest achievable Gaussicity for the horn,

$$\frac{\partial\eta_{coupling}}{\partial\frac{w_A}{a}} = 0, \qquad \eta_{coupling} = \frac{P_{00}^{co}}{P_{tot}}. \tag{2.3.22}$$

The optimum ratio of $\frac{w_A}{a} = 0.8632$ gives the maximum coupling $\eta_{coupling} = 0.932$ to the fundamental mode. Another important factor to consider is the polarisation efficiency ϵ_{pol}, which is calculated using the electric field distribution at the aperture,

$$\epsilon_{pol} = \frac{\iint |E_v|^2\,dv\,du}{\iint |E_v|^2 + |E_u|^2\,dv\,du} = 0.905. \tag{2.3.23}$$

The overall coupling to a Gaussian beam is equivalent to the Gaussicity [7],

$$\epsilon_G = \eta_{coupling}\cdot\epsilon_{pol} = 0.932\cdot 0.905 = 0.843 = 84.3\ \%. \tag{2.3.24}$$

Therefore, the highest achievable Gaussicity of the diagonal horn is 84%, which is sufficient for coupling to an optical source.

2.3.2 Pyramidal horn antenna

The pyramidal horn, also known as the rectangular horn, is one of the most widely used horns. It is characterised by being flared in both directions, unlike E and H-plane sectoral horns. Its radiation characteristics are, in principle, a combination of the two sectoral horns. While harder than the diagonal horn, the pyramidal horn is also relatively simple to drill using CNC milling, making it an attractive option for supra-THz frequencies. The pyramidal horn being essentially a flared rectangular waveguide leads to it having the following electric field at the aperture:

$$E_{ap} = \hat{y}\ E_0\ cos\left(\frac{\pi x}{2a}\right)e^{-j[k(x^2/\rho_2 + y/\rho_1)]}. \tag{2.3.25}$$

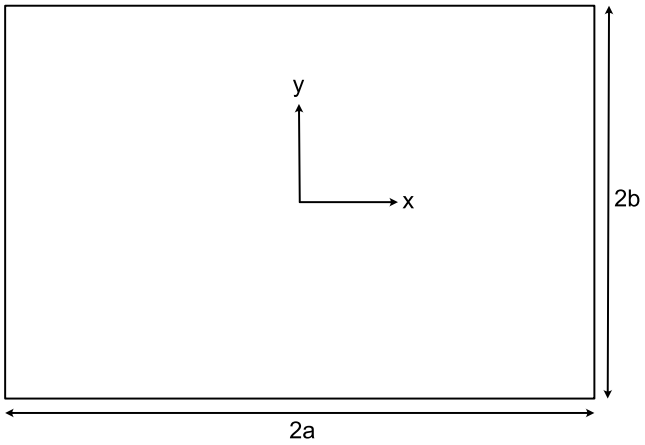

Figure 2.5: Aperture geometry of a pyramidal horn antenna.

Inserting the aperture field into equation 2.3.19 gives the following expression:

$$\frac{P_{mn}}{P_{tot}} = \frac{2}{\pi}\frac{a^2}{w_A^2}\frac{\left|\int_{-1}^{1}\int_{-b/a}^{b/a} cos(\frac{\pi u}{2})\, H_m\left[\frac{2au}{w_A}\right] H_n\left[\frac{2au}{w_A}\right]\, dv\, du\right|^2}{\int_{-1}^{1}\int_{-b/a}^{b/a}\left|cos(\frac{\pi u}{2})\right|^2 dv\, du}. \tag{2.3.26}$$

Just like for the diagonal horn, the $\frac{w_A}{a}$ ratio is arbitrary. The additional variable here is the $\frac{b}{a}$ fraction which is an antenna design choice that can affect the antenna properties. Since the polarisation factor of the pyramidal horn is $\epsilon_{pol} = 1$, the coupling factor is, therefore, equal to the Gausscity in this case. The maximum fundamental mode coupling, $\epsilon_G = 0.88$, is achieved for $\frac{b}{a} = 0.7$ and $\frac{w_A}{a} = 0.7$, as seen in Figure 2.6.

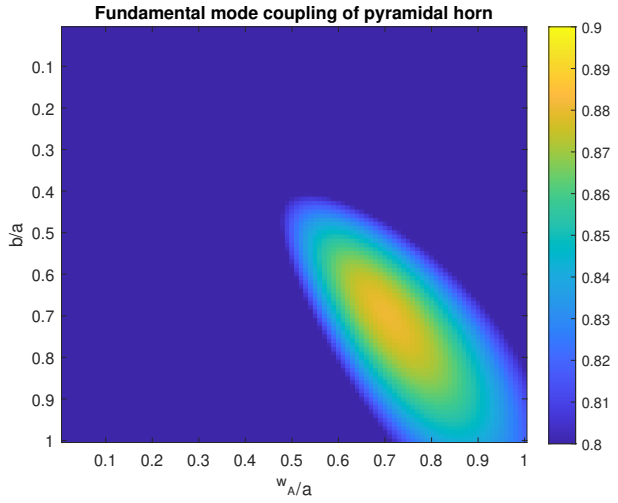

Figure 2.6: Gaussicity of the pyramidal horn in respect to the $\frac{b}{a}$ and $\frac{w_A}{a}$ ratios.

2.3.3 Diagonal-spline horn antenna

The smooth-walled spline-profiled horn was introduced in 2002 by Granet *et al.* [26]. The horn was demonstrated in the W-band and had a Gaussicity competitive with the corrugated horn. While the machining of the smooth-walled spline horn is easier than its corrugated counterpart, it is still non-trivial due to the steps needed to form the cubic spline shape of the horn. Hence, in 2018 Gibson *et al.* [11] combined the spline horn with the easily fabricated diagonal horn to make a new horn, easier to fabricate for THz applications. A more simplified version of it was demonstrated by Monotfre in 2019 [27], which is referred to in this work as the diagonal-spline horn. Unlike other smooth-wall profiles, the diagonal-spline consists of 9 nodes connected by straight lines to form the smooth-wall variable profile. The diagonal-spline was demonstrated to have a crosspolar level below -20 dB and a Gaussicity above 96%. However, the feasibility of accurately machining the diagonal-spline horn for supra-THz applications is yet to be explored.

2.4 Antenna measurements

The antenna radiates electromagnetic fields that change distribution depending on the distance travelled [21]. The different fields are categorised into three regions: Reactive near-region, radiating near-field and far-field as demonstrated in Figure 2.7. The three regions can be described in the following manner:

Reactive near-field region: The region surrounding the aperture of the antenna, which is dominated by the reactive fields. The electric and magnetic fields are not guaranteed to be in phase with each other, and the field distribution is highly dependent on the distance to the antenna. The region spans from the aperture to the distance $0.62\sqrt{\frac{D^3}{\lambda}}$, where D is the largest dimension of the antenna.
Radiating near-field region: The region is also known as the Fresnel region. The radiation fields dominate over the reactive ones in this region, the electric and magnetic fields are in phase, but the field distribution is still dependent on the distance from the antenna. The Fresnel region spans from the distance $0.62\sqrt{\frac{D^3}{\lambda}}$ to the distance $2\frac{D^2}{\lambda}$.
Far-field region: Here, the field distribution is independent of the distance, and the field can be approximated as spherical wave-fronts. Due to the large distance from the antenna, it is effectively a point source, and its size and shape can be neglected.

2.4.1 Near-field measurement

The far-field characteristics can be attained by making measurements in the near-field and then using analytical methods to transform the measured near-field data. This method is known as Near-Field to Far-Field (NF/FF) transformation. The measurement can be performed by scanning a probe over a surface, such as a plane, a cylinder, or a sphere. The planar scan option makes the measurements more compact and reduces requirements on motorised stages. Generally, NF/FF transformation techniques are based on measurements of the magnitude and phase of the

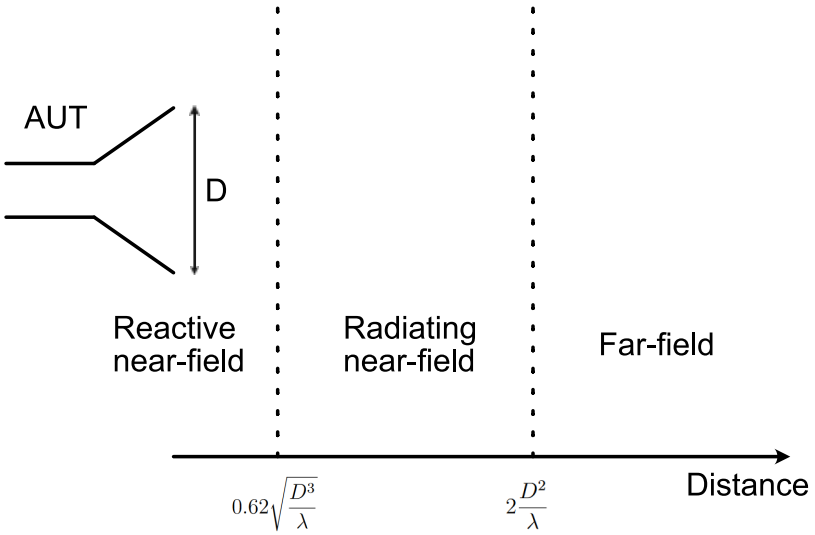

Figure 2.7: Illustration of the different regions for an antenna under test.

tangential electric field components radiated by the Antenna Under Test (AUT) at regular intervals of $\Delta x = \Delta y = \frac{\lambda}{2}$, over a defined plane in the near-field orthogonal to the direction of propagation. Planar NF/FF techniques are well suited for measuring antennas with low back lobes, including directional antennas such as the horn antennas used in this thesis.

2.4.1.1 Modal expansion method for planar systems

The planar NF/FF is mathematically based on the plane wave expansion using Fourier transform techniques [28]. Any arbitrary monochromatic wave can be regarded as a superposition of plane waves of the same frequency travelling in different directions, with different amplitudes. The modal expansion method aims to find the plane waves' unknown amplitudes and directions of propagation. The relationship between the near-field E-field measurements and the far-field for planar systems can be represented by:

$$\mathbf{E}(x,y,z) = \frac{1}{4\pi^2}\int_{-\infty}^{\infty}\int_{-\infty}^{\infty}\mathbf{f}(k_x,k_y)e^{-j\mathbf{k}\cdot\mathbf{r}}\,dk_x dk_y, \tag{2.4.27}$$

where

$$\mathbf{f}(k_x,k_y) = \hat{\mathbf{a}}_x f_x(k_x,k_y) + \hat{\mathbf{a}}_y f_y(k_x,k_y) + \hat{\mathbf{a}}_z f_z(k_x,k_y) \tag{2.4.28}$$

$$\mathbf{k} = \hat{\mathbf{a}}_x k_x + \hat{\mathbf{a}}_y k_y + \hat{\mathbf{a}}_z k_z \tag{2.4.29}$$

$$\mathbf{r} = \hat{\mathbf{a}}_x x + \hat{\mathbf{a}}_y y + \hat{\mathbf{a}}_z z. \tag{2.4.30}$$

The plane wave spectrum of the field $\mathbf{f}(k_x, k_y)$ are given by:

$$f_x(k_x, k_y) = \int_{-b/2}^{b/2} \int_{-a/2}^{a/2} E_{x0}(x', y', z' = 0) e^{j(k_x x' + k_y y')}\, dx'\, dy' \tag{2.4.31}$$

$$f_y(k_x, k_y) = \int_{-b/2}^{b/2} \int_{-a/2}^{a/2} E_{y0}(x', y', z' = 0) e^{j(k_x x' + k_y y')}\, dx'\, dy'. \tag{2.4.32}$$

The plane wave spectrum function $\mathbf{f}$ can be used to obtain the far-field pattern of the antenna,

$$\mathbf{E}(r, \theta, \Phi) \approx j \frac{k e^{-jkr}}{2\pi r} [\mathbf{f}(k_x, k_y)\, cos(\theta)]. \tag{2.4.33}$$

3
Method

This chapter starts with an overview of the Ansys HFSS simulation software. The second section presents the different horn models and discusses their differences. The chapter also includes the machining of the diagonal horn and concludes with the set-up procedure of the measurement system.

3.1 Full electromagnetic simulation of the horns

Electromagnetic simulation software is used to simulate the effect of split-block misalignment on the horn antennas. The software used in this thesis is Ansys HFSS, which solves the electrical and magnetic field of the antenna by attempting to solve Maxwell's equations in differential form numerically. Multiple mathematical methods exist as solvers. The most widely used one is FEM, based on Maxwell's curl equations and used in the frequency domain. The specifications used for the simulations were the maximum accepted difference in S-parameters between two iterations δS and the sweep type. To have an accurate simulation, ΔS should be close to zero, but the closer it is, the more mesh is added to each iteration, making it computationally intensive.
The horns were all simulated with a maximum $\Delta S = 0.01$ and an interpolating sweep of 401 points over the WM-570 (WR2.2) band. The interpolating sweep is used instead of the more accurate discrete sweep since it is less time-consuming while remaining sufficiently accurate. The material used for the waveguide walls is brass with an electrical conductivity of $\sigma = 15 \times 10^6$ S/m. The horn aperture in the model is surrounded by a Perfect Electric Conductor (PEC) surface to emulate the aperture of a split-block configuration. Additionally, a vacuum box is placed around the models' horn apertures. The box has its faces set as radiation boundaries to absorb the radiated field and model the far-field region.
The complete model has to be simulated for the misaligned cases as there is an asymmetry in the model. Wave ports are used to compute the S-parameters as they are preferred for enclosed geometries like waveguides. The horns are designed for centre frequency 415 GHz, due to its proximity to the middle of the band. The solution frequencies are set to 360, 415 and 470 GHz to highlight the difference in the antennas' characteristics over the band. The Gaussicity is calculated from the simulated electric field at the aperture of the horn. Using the definition of Gaussicity in equation 2.2.11, the electric field is extracted from Ansys HFSS using a MATLAB script, see section A.1 in Appendix A.

3.1.1 Diagonal horn antenna

The diagonal horn antenna model, seen in Figure 3.1a, is made by creating a square surface at a distance L from a rectangular waveguide. The square is rotated by 45° along the Z-axis and extruded towards the waveguide with a negative flare angle. The flare angle is calculated so the extrusion converges into a point at a distance L.

The far-field pattern of the simulated diagonal horn can be seen in Figure 3.1b. The symmetrical property of the diagonal horn can be observed since the three radiation patterns align well at the boresight. Further away at $\theta = 18\,°$, the D-plane has side lobes of -16 dB. The crosspolar is significant in the D-plane, where it has a maximum of -16 dB at $\theta = 13\,°$.

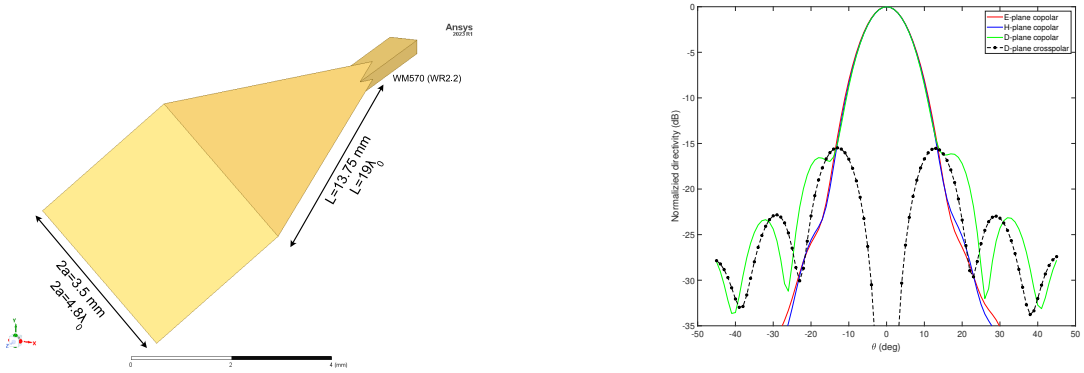

(a) **(b)**

Figure 3.1: a) 3D-EM model of the diagonal horn antenna, designed for centre frequency 415 GHz. b) Normalised far-field pattern of the diagonal horn at 415 GHz in the E, H and D-planes.

3.1.2 Pyramidal horn antenna

The pyramidal horn model, seen in Figure 3.2a, is designed for the optimum Gaussicity as shown in section 2.3.2, with $\frac{b}{a} = 0.7$. The size of the aperture is chosen to get a similar directivity to the other horns, as it would make a more explicit comparison. The pyramidal model is made by creating a rectangular surface with dimensions a and b at a distance L from the waveguide and connecting the surface with the waveguide.

Compared to the diagonal horn, the pyramidal has crosspolar levels below -40 dB in the E, H, and D planes. However, as seen in Figure 3.2b, the radiation pattern is not as symmetrical due to the differences in the E and H planes.

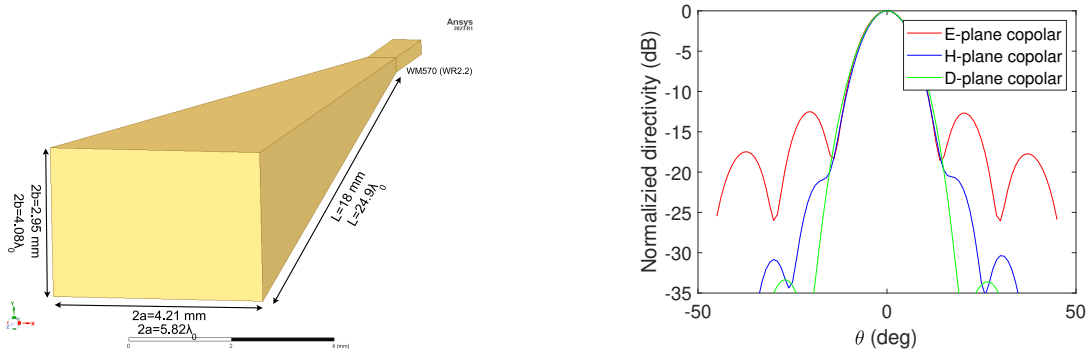

(a) **(b)**

Figure 3.2: a) 3D-EM model of the pyramidal horn antenna, designed for centre frequency 415 GHz. b) Normalised far-field pattern of the pyramidal horn at 415 GHz in the *E*, *H* and *D*-planes.

3.1.3 Diagonal-spline

The diagonal-spline horn model, seen in Figure 3.3a, is made according to the method in [27], with nine nodes to define the variable profile. This design has a larger flare angle at the throat, which decreases the generated phase shift from the split-block misalignment. Additionally, the rectangular waveguide is flared to a square form as it transitions to the horn. The flaring of the waveguide is done to reduce reflection losses as advised by Gibson *et al.* [11]. The model of the diagonal-spline is done by creating a polyline with nine nodes, as seen in Table 3.1. Two additional lines are added to create a surface from the polyline. The surface is then rotated by 90 degrees around the z-axis. The two surfaces are connected using straight lines, forming closed rectangles between the nodes.

Table 3.1: Nodes used to create the polyline form of the diagonal-spline.

i	z_i (mm)	y_i (mm)
1	1.46	0.61
2	3.22	1.10
3	4.74	1.38
4	5.91	1.49
5	7.26	1.50
6	8.67	1.53
7	11.42	1.72
8	13.64	2.10
9	16.10	2.49

The resulting figure is mirrored until a complete aperture is obtained. Then, the polynomial figure is joined with the flared rectangular waveguide to form the diagonal-spline model seen in Figure 3.3a.

Figure 3.3b shows a more symmetrical radiation pattern compared to the diagonal and pyramidal horns. The three radiation patterns are aligned up to $\theta = \pm 20°$.

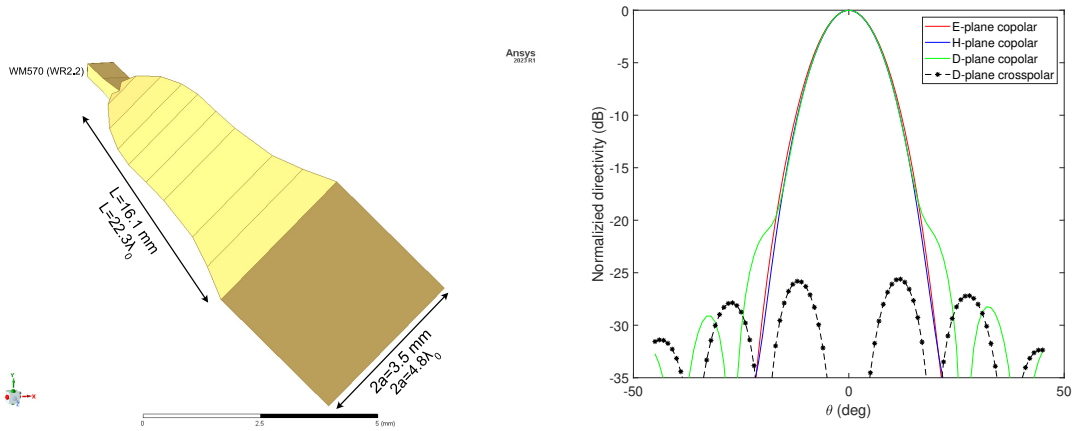

(a) **(b)**

Figure 3.3: a) 3D-EM model of the diagonal-spline horn antenna, designed for centre frequency 415 GHz. b) Normalised far-field pattern of the diagonal-spline horn at 415 GHz in the E, H and D-planes.

3.1.4 Comparison of the three horns

The characteristics of the three horns at 415 GHz are presented in Table 3.2. The phase centre location (PCL) is obtained using HFSS by sweeping the source point of the far-field radiation to find the minimum phase change in a plane. The optimum value of $\frac{w}{a}$ is obtained by finding which value maximises the Gaussicity from the simulated aperture fields.

Table 3.2: Table of some relevant characteristics of the simulated horn antennas at 415 GHz. The PCL is calculated in the H and E-planes and the crosspolar is normalised to the directivity of the respective horn.

Horn antenna	Length (λ)	PCL [H/E] (mm)	Directivity (dBi)	Crosspolar (dB)	w/a	Gaussicity (%)
Diagonal	19	2.35/2.4	23.3	<-15.9	0.86	85
Pyramidal	24.9	2.45/2.2	23.4	<-43.0	0.35	88
Diagonal-spline	22.3	1.7/1.1	23.1	<-25.5	0.73	96

3.2 Split-block misalignment

The split-block misalignment is a significant error source for some horn antennas at supra-THz. Due to the difficulty of keeping the misalignment below a few micrometres, the misalignment is significant enough to affect the horn antenna's performance. The misalignment's effect on the diagonal horn antennas can be seen in Figure 3.4.

The figure shows how the linear polarisation of the horn degrades once a split-block misalignment is introduced into the electromagnetic model.

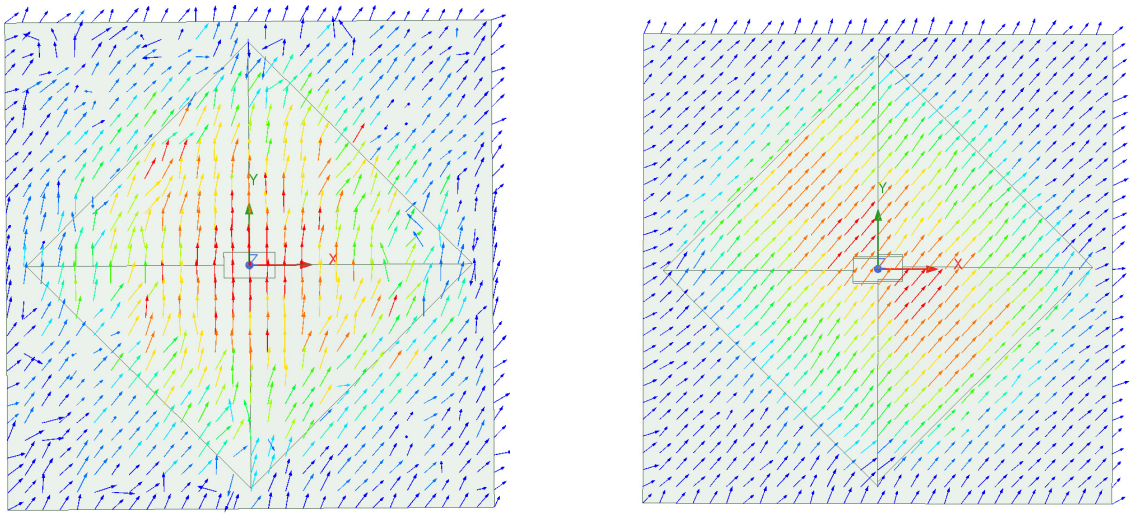

(a) Aligned **(b)** Misaligned

Figure 3.4: Magnitude of the complex electric field at the aperture for the aligned and misaligned diagonal horn antenna.

This explains the increase in crosspolar that Hammar *et al.* noted in their measurements. The misalignment is investigated, and a theoretical model of the misalignment's effect on the Gaussicity is provided with the simulation results for comparison.

3.2.1 Theoretical model

The diagonal horn antenna has the TE_{10} and the TE_{01} modes propagating through it as mentioned in 2.3.1. For the aligned case, these two modes experience the same side length and have, therefore, the same propagation factor β. The superposition of the two modes creates the linearly polarised output required from the horn antenna. However, once the split-block misalignment is introduced, the geometry inside the horn antennas changes. As one side effectively becomes Δa narrower, the other side becomes Δa wider, as seen in Figure 3.5. This change leads to the two modes having different propagation factors, creating a phase shift with respect to the distance travelled. Stenarson *et al.* [29] have presented a similar analysis where a slight difference in the waveguide's width of calibration material can lead to an inaccurate calibration due to a change in β.

The phase shift for a misaligned rotated square waveguide can be presented using the phase propagation term $e^{-j\beta_i z}$, where i is an index for the mode. To calculate β_i, the side length change Δa for a certain misalignment has to be known. Figure 3.5 shows the trigonometry used to calculate $\Delta a = \Delta y/\sqrt{2}$.

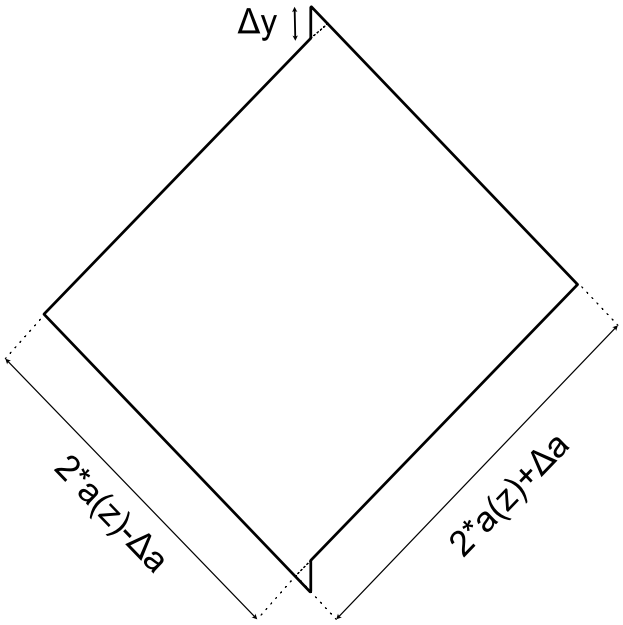

Figure 3.5: Illustration of the split-block misalignment on the diagonal horn's aperture. The misalignment effectively changes the side lengths with $\pm\Delta a$.

Having the waveguide dimensions for a certain misalignment makes it possible to calculate the propagation factor,

$$\beta_{ij} = \sqrt{k^2 - k_{c_{i,j}}}, \tag{3.2.1}$$

where $k_{c_{i,j}}$ is the wavenumber corresponding to the mode i, j and is given by:

$$k_{c_{i,j}} = \left[\left(\frac{i\pi}{a}\right)^2 + \left(\frac{j\pi}{a}\right)^2\right]^{\frac{1}{2}}. \tag{3.2.2}$$

A rectangular waveguide is assumed to excite a non-flared diagonal waveguide to study the phase shift between the two modes. The two modes will have the following phase shift after propagating a distance z:

$$\Delta\theta(\Delta y) = \left|z \cdot (\beta_{10} - \beta_{01})\right| \tag{3.2.3}$$

$$= \left|z \cdot \left(\sqrt{k^2 - \frac{\pi}{a + \Delta a}} - \sqrt{k^2 - \frac{\pi}{a - \Delta a}}\right)\right| \tag{3.2.4}$$

$$= \left|z \cdot \left(\sqrt{k^2 - \frac{\pi}{a + \frac{\Delta y}{2}}} - \sqrt{k^2 - \frac{\pi}{a - \frac{\Delta y}{2}}}\right)\right|. \tag{3.2.5}$$

However, the diagonal horn is flared, which means the side length a is not constant. Therefore, the diagonal horn is divided into small waveguide sections of length dz and side length $a(z') = a_0 + \theta \cdot z'$, where θ is the flare angle of the horn. By summing the phase shifts over the small waveguide sections, a total phase shift by the aperture

can be calculated in the following manner:

$$\Delta\theta(\Delta y) = \sum_m \left| dz \cdot (\beta_{10}(m) - \beta_{01}(m)) \right| \tag{3.2.6}$$

$$= \sum_m \left| dz \cdot \left(\sqrt{k^2 - \frac{\pi}{a(m) + \Delta a}} - \sqrt{k^2 - \frac{\pi}{a(m) - \Delta a}} \right) \right| \tag{3.2.7}$$

$$= \sum_m \left| dz \cdot \left(\sqrt{k^2 - \frac{\pi}{a(m) + \frac{\Delta y}{2}}} - \sqrt{k^2 - \frac{\pi}{a(m) - \frac{\Delta y}{2}}} \right) \right|, \tag{3.2.8}$$

where the side length is $a(m) = a_0 + \theta \cdot m \cdot dz$. As $a(m)$ increases, $\beta_{10}(m)$ and $\beta_{01}(m)$ will be converging to the same value, meaning the phase shift is mostly generated near the throat. The flare angle determines how quickly the propagation factors converge and is an important parameter to consider when designing the diagonal horn.

The phase shift is not the only consequence of the misalignment; the mode power distribution is also affected. According to simulations, the two modes receive a different amount of power from the rectangular waveguide. In an aligned case, the two modes receive an equal (or close to equal) power amount. This has been characterised by Withington and Murphy using the power balance factor $\Omega = \left(\frac{E_y}{E_x}\right)^2$ [30]. The power balance factor's dependency on the misalignment was extracted by having a second port at the diagonal horn's aperture with two modes set to align with the TE_{10} and TE_{01} modes. The difference in power received by the two modes was plotted against the swept misalignment, and a linear relation $\Omega(\Delta y)$ was extracted based on the data, as seen in Figure 3.6.

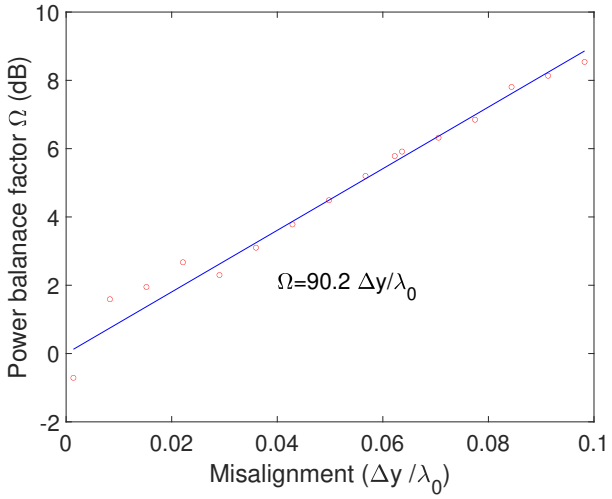

Figure 3.6: Simulated power balance factor respective to the misalignment.

The electric field distribution seen in equation 2.3.14 is adjusted to match the mis-

alignment.

$$E_\eta(\Delta y) = \hat{\eta} \cdot \mathbf{E}_{ap} = \frac{E_0}{\sqrt{2}} \left[cos\left(\frac{\pi(\eta - \xi)}{2\sqrt{2}a} \right) + \sqrt{\Omega(\Delta y)}\, cos\left(\frac{\pi(\eta + \xi)}{2\sqrt{2}a} + \Delta\theta(\Delta y) \right) \right] e^{jk\delta} \quad (3.2.9)$$

The copolar electric field at the aperture E_η is dependent on the phase shift and the power balance factor, which are affected by the misalignment Δy. Therefore, the total Gaussian coupling factor ϵ_G, which is expressed in terms of E_η in equation 2.3.24, can be calculated with respect to misalignment Δy. The diagonal horn's decrease in Gaussicity is, therefore, given by:

$$\epsilon_G(\Delta y) = \epsilon_{coupling}\Big(E_\eta\big(\Delta\theta(\Delta y), \Omega(\Delta y)\big)\Big) \cdot \epsilon_{pol}\Big(E_\eta\big(\Delta\theta(\Delta y), \Omega(\Delta y)\big)\Big). \quad (3.2.10)$$

3.2.2 Misalignment in electromagnetic models

The horn antenna models in HFSS are misaligned along with the rectangular waveguide to emulate the split-block misalignment, as seen in Figure 3.7. The misalignment is done by splitting the model along the zy-plane and vertically (y-axis) shifting the two halves by $\frac{\Delta y}{2}$ and $-\frac{\Delta y}{2}$, respectively.

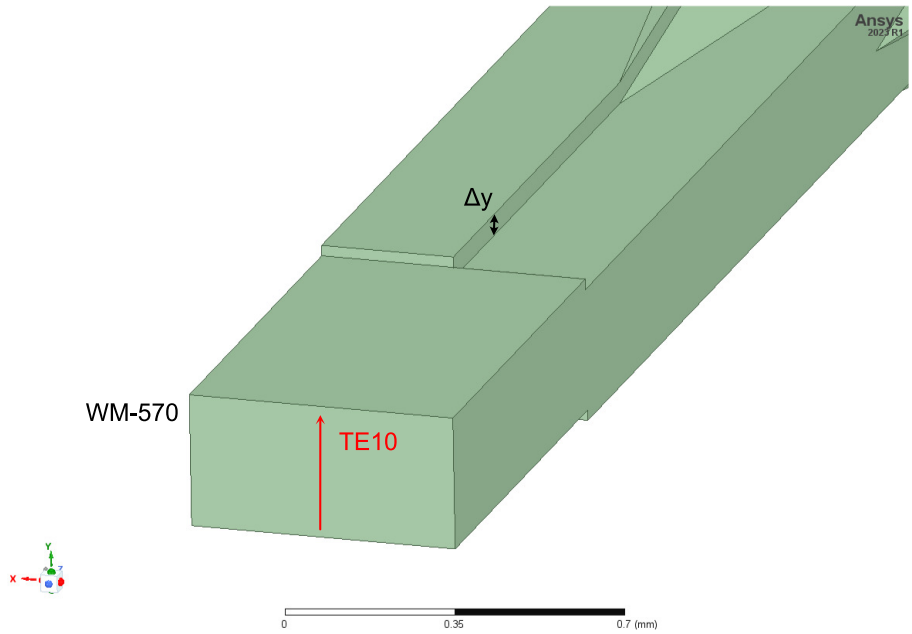

Figure 3.7: Misaligned 3D-EM model of the diagonal horn antenna.

3.3 High-precision machining

To experimentally verify the misalignment's effect on the diagonal horn, the split-block diagonal is realised using CNC milling. Therefore, a split-block with different alignment cases is desired to reduce the required machining. A mechanical model of

the diagonal horn is designed using the solid computer-aided design (CAD) software SOLIDWORKS. The block is designed with a UG-387 flange to enable integration with the WM-570 extenders used for the measurements. The dimensions of the horn are equal to the ones used in the 3D-EM simulations for an accurate comparison between the measurements and the simulations. The different alignment cases were introduced by having three pairs of dowel holes for alignment. In the bottom block, the alignment holes are laterally shifted with 11 μm. In the top block, the holes are laterally shifted with the same amount in the opposite direction. By inserting dowel pins in one of the dowel hole pairs, the alignment of the split-blocks can be set to either: aligned, $\frac{22\,\mu\text{m}}{\lambda_0} = 3\%$ misaligned, or $\frac{44\,\mu\text{m}}{\lambda_0} = 6\%$ misaligned, see Figure A.2 in Appendix A for a sketch of the design. Two screw hole pairs are available for each alignment case, ensuring good contact between the block.

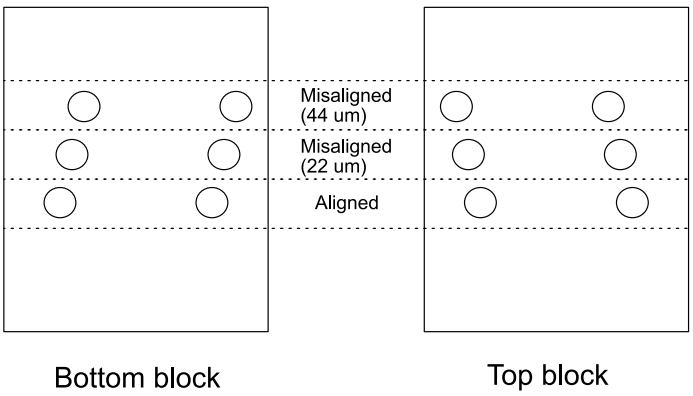

Figure 3.8: Illustration of two split-blocks in a top-down perspective. Placing the alignment pins in one of the three pairs sets the *E*-plane alignment of the block.

Based on the mechanical design, a brass piece of metal is machined into the split-blocks using a KERN Micro HD machine. The complete block can be seen in its aligned state in Figure 3.9. The horn aperture is chamfered with 20 degrees to reduce possible standing wave effects. However, the surface is kept flat at 0.3 mm around the aperture.

The alignment of the split-blocks is observed using a Nikon LV150 microscope with an attached camera. The alignment agrees well with the expected values according to the mechanical design.

3.4 Measurement setup

Characterising the horn antenna is achieved by measuring it in the near-field or the far-field. The far-field measurements require rotational stages to obtain the radiation pattern. Moreover, the cable flexing caused by rotating an extender is more significant than xy-planar movement. A planar scan using two linear motorised stages is sufficient for the near-field measurement. The near-field radiation pattern

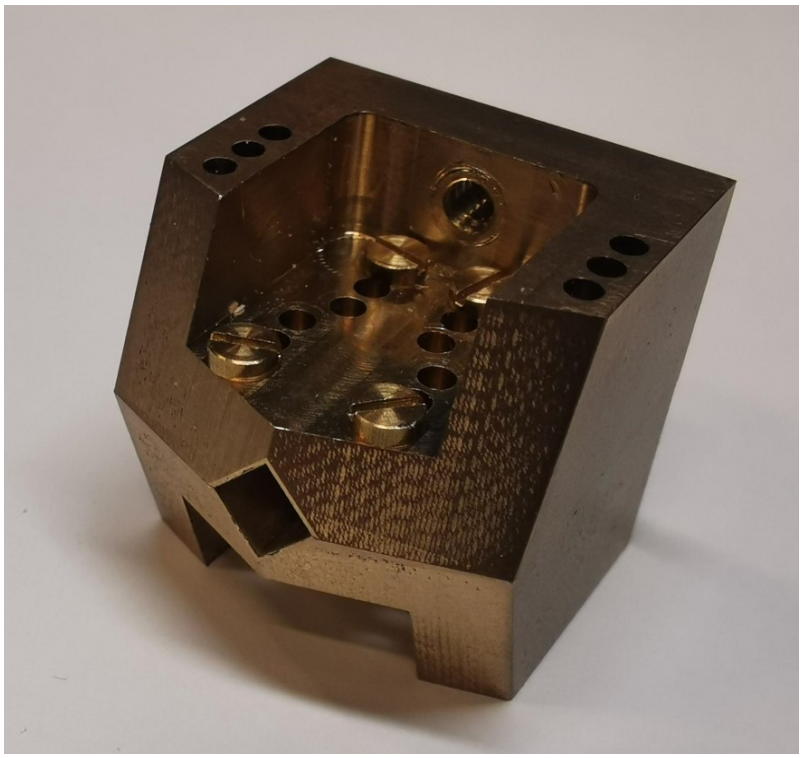

Figure 3.9: Picture of the complete brass diagonal horn block.

is measured and Fourier transformed into the far-field radiation pattern using the modal expansion method presented in section 2.4.1.1.

The setup consists mainly of two motorised linear stages, a motor controller, two WM-570 extenders, a Vector Network Analyser (VNA), absorbers, a Personal Computer (PC), a vibration-free optical bench and components. The motor stages and an optical support rod are mounted on the optical bench, ensuring they are in parallel planes. The extenders are mounted on custom-made platforms (machined using CNC milling) that connect the extender to a breadboard mounting. A 90 degrees breadboard mounting is used to mount the extender platforms to the motor stages and the optical support rod. A spirit level ensures that the platforms' surfaces are horizontal. The extenders are mounted on the platforms, enabling the motor controller to adjust port one on the positioning system into the same xy-position as the stationary port two, see Figure 3.10. Once a through connection is made between the ports, optical bench components are mounted to restrict the movement of the optical support rod in the x-direction, only allowing movement in the z-direction. The Keysight PNA is connected to the extenders and calibrated using SOLT. An open-ended waveguide aperture antenna by Dahlbäck *et al.* [31] is used as an antenna probe for near-field measurements. The probe is mounted with an absorber on the linear stages, while the diagonal horn is connected to the stationary port. A distance of 15 mm is kept between the antennas since the radiating near-field region is 8-29 mm.

The horn antenna's boresight has to be accurately located to start a measurement.

Therefore, a phase detection scheme is employed to find the location where the magnitude of the unwrapped phase is minimised [32]. A PC using LabVIEW code communicates with the motor controller and the VNA. The LabVIEW code aims to find the minimum phase in the x-direction, move to that location, and sweep the y-direction to find the boresight, as seen in Figure 3.11. The boresight is set as the grid's origin, and the setup is ready for the near-field measurement.

The measurement process is automated through the LabVIEW code to measure the magnitude and phase of the S-parameters at each grid point the motor controller moves to. At the start of the process, a reference measurement is taken at the boresight before moving to a corner of the grid. Samples are taken in the x-direction (horizontally) for a fixed y-value. Once a row of the grid is measured, the probe moves back to the boresight to take another reference measurement before continuing. The reference measurements are compared to the first measurement and used to compensate for the amplitude and phase drifts that occur during the measurement.

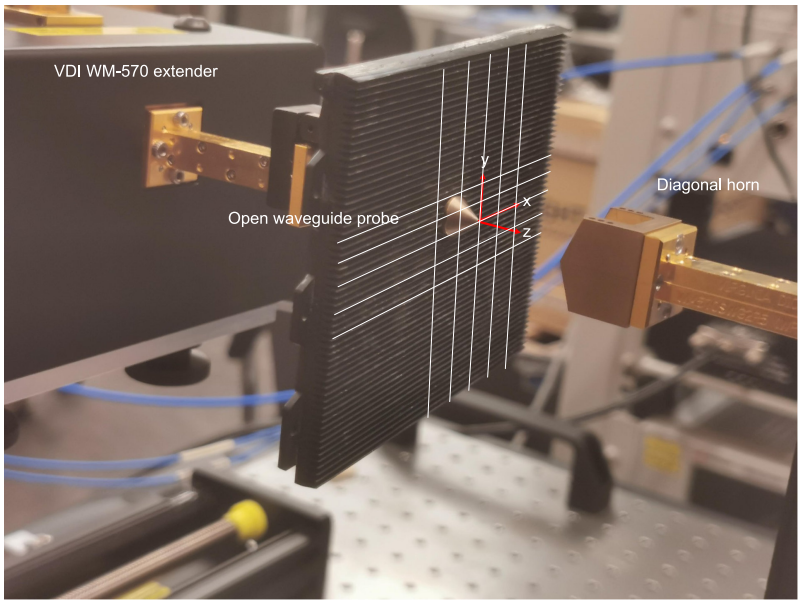

Figure 3.10: Picture showing the open waveguide probe in the xy-plane. The extender for port 1 is mounted on a custom-made platform. In the bottom left corner, a motorised stage can be seen.

The parameters to consider for the measurement are the step size, grid size, IF bandwidth and the distance between the antennas. The step size is $<\frac{\lambda}{2}$ to avoid any spectral aliases in the far-field pattern. Therefore, the grid size decides the area covered by the probe, and since a 40 dB dynamic range is required, it is crucial to pick an appropriately large grid size. The LabVIEW code delays the S-parameter measurement until a sweep is completed, and since the IF bandwidth decides the sweep time, it is a significant factor in the measurement time.

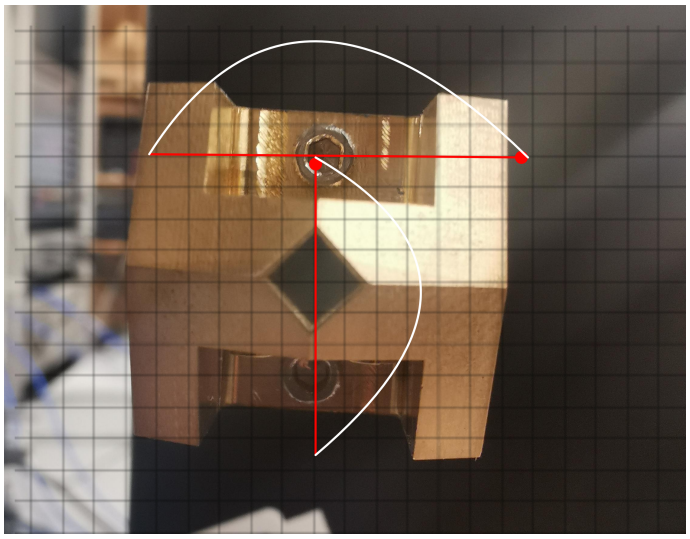

Figure 3.11: Alignment system used for the probe to find the boresight of the horn antenna. The unwrapped phase is measured in a horizontal and vertical scan to find the optimal location.

The measurement of an antenna under test (AUT) consists of two parts: the copolar and the crosspolar measurement. For the crosspolar, the extender is mounted directly on the supporting rod, effectively rotating the horn antenna around the z-axis with approximately 90°. The rotation is controlled with a spirit level. However, fine rotational adjustments are not available in the setup.

4

Results

This chapter presents the results obtained from the measurements along with the simulations. The stability of the measurement setup is shown. The near-field pattern is presented as it was measured, in a planar xy-grid. In contrast, the far-field radiation pattern is illustrated using the E, H and D-planes and compared with the respective simulation result. Finally, the deterioration of the copolar directivity, crosspolar level and Gaussicity with misalignment is presented for the three horn antennas to evaluate their sensitivity.

4.1 Measurement results

The measurements were done at 360 GHz since the open waveguide probe is designed for the WM-710 band (260-400 GHz). The majority of the measurement time is based on the wait time set by the code. As this measurement uses an IF bandwidth of 500 Hz, the wait time before a sample is taken is set to two seconds. The reference samples taken to compensate for the phase and magnitude drift can be seen in Figure 4.1. During the measurement, the magnitude drift is $|m| < 0.015$ dB, while the phase drift is $|p| < 0.06$ dB.

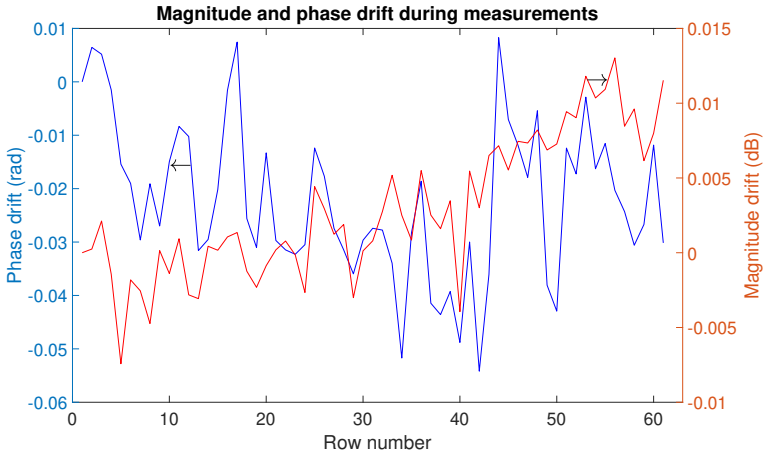

Figure 4.1: Magnitude and phase drift of S_{21} with each row.

The return loss of the machined diagonal horn is <-20 dB which is sufficiently good. A comparison of the return loss for the aligned and misaligned cases can be seen in Figure 4.2. The misalignment does not have a significant impact on the return loss that can be observed over the whole band.

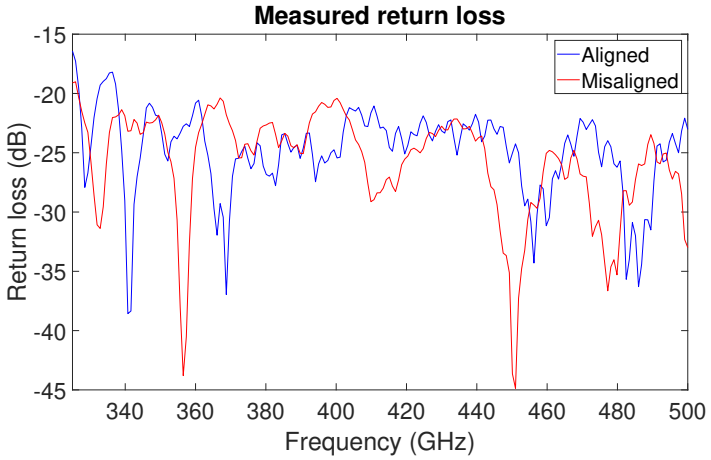

Figure 4.2: Measured return loss of the aligned and 6% misaligned cases.

The probe alignment uses the phase detection scheme with a 50 μm step size. The sampled plan consists of 61x61 points, which is large enough to get a dynamic range larger than 35 dB in the near-field radiation pattern, as seen in Figure 4.3. The step size used is $\Delta x = 375\ \mu$m which is $< \frac{\lambda}{2}$ at 360 GHz.

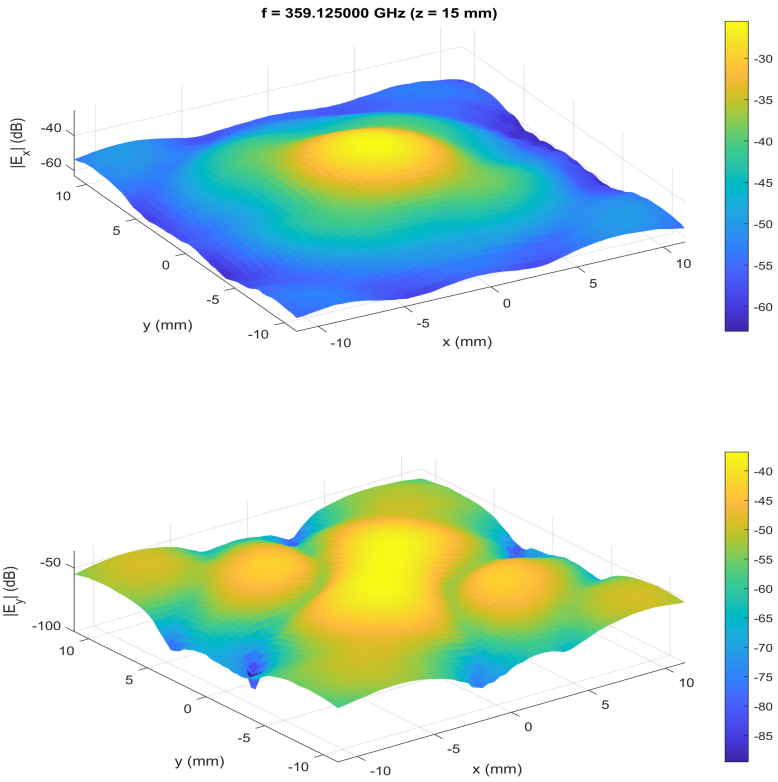

Figure 4.3: Measured magnitude of S_{21} for the copolar (up) and the crosspolar (down) at $z = 15$ mm.

The measured far-field radiation pattern for the aligned diagonal horn is represented using the E, H and D-planes in Figure 4.4. The crosspolar plots in the E and H-planes can't be seen as they are <-35 dB. The measured crosspolar in the D-plane is <-12 dB, which is larger than expected from simulations and theory. The disparity is most likely due to the restrictions in the setup. The open waveguide is not an ideal probe and likely not in an ideal orthogonal position to the AUT. Therefore, the probe is susceptible to registering a higher crosspolar signal than expected at the boresight, where maximum power is radiated.

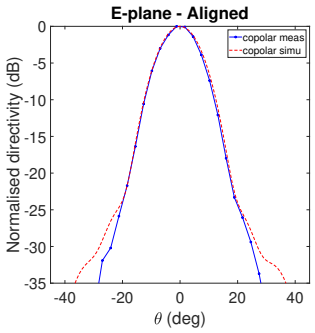

(a) Copolar in the E-plane.

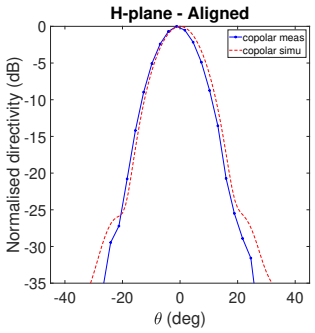

(b) Copolar in the H-plane.

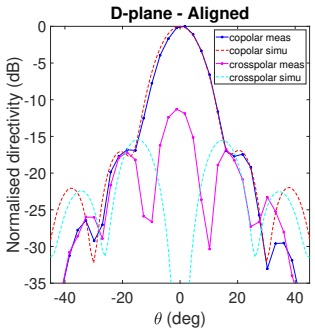

(c) Copolar and crosspolar in the D-plane.

Figure 4.4: Measured and simulated radiation pattern of the aligned diagonal horn at 360 GHz.

The measured and simulated radiation pattern of the 6% misaligned horn can be seen in Figure 4.5. The crosspolar is >-5 dB in all three planes and has a Gaussian form. The measurements of the crosspolar are 2-3 dB larger than the simulations. This is likely due to the angle uncertainty mentioned previously.

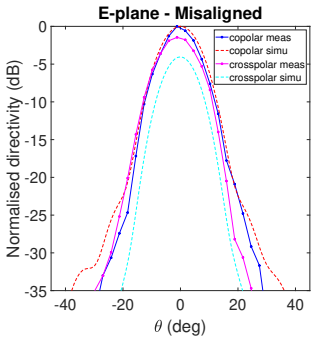

(a) Copolar and crosspolar in the E-plane.

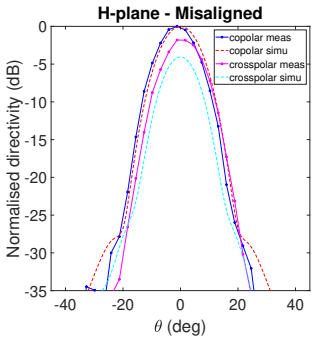

(b) Copolar and crosspolar in the H-plane.

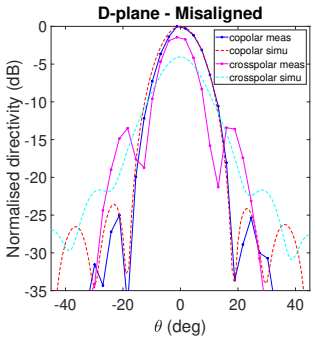

(c) Copolar and crosspolar in the D-plane.

Figure 4.5: Measured and simulated radiation pattern of the 6% misaligned diagonal horn at 360 GHz.

The radiation patterns in Figure 4.5 are normalised to the respective maximum copolar directivity. However, the copolar directivity of the horn antenna is decreased

when misaligned. Figure 4.6 shows a decrease of 2 dB in copolar directivity when the diagonal horn is misaligned by 6% of the wavelength.

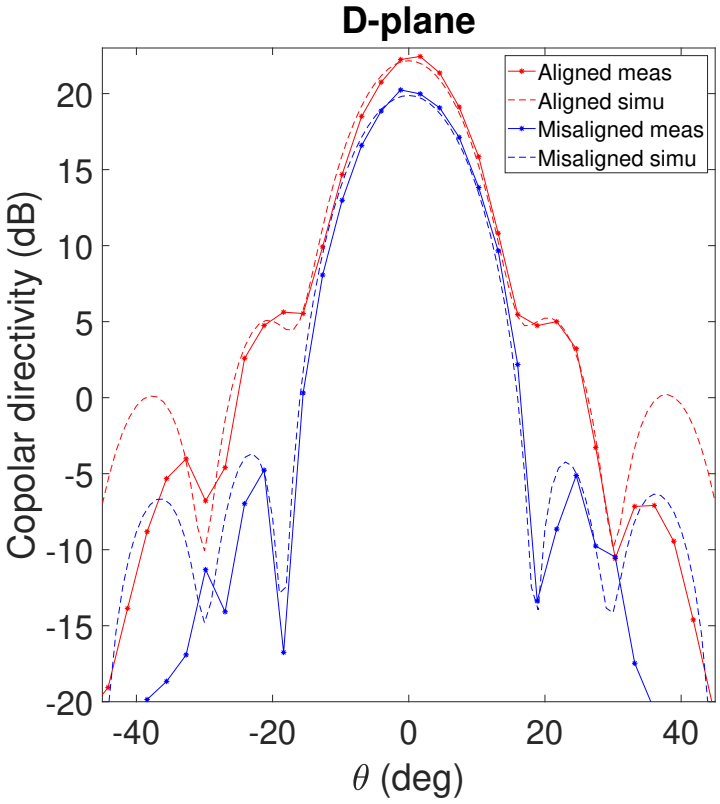

Figure 4.6: Measured and simulated copolar directivity of the aligned and 6% misaligned diagonal horn antenna in the *D*-plane.

4.2 Simulation comparison of three typical horns

The misalignment introduced to the simulations is based on the expected equivalent at 4.7 THz, which is ± 2 μm due to the errors in the alignment and fabrication processes. Therefore, the expected misalignment $\Delta y = 0.031\lambda$ is of interest. Additionally, the extreme case of 0.062λ is investigated to check the sensitivity of the different horns and how well the simulation results agree with expected models based on theory. The comparison is performed at 360, 415 and 570 GHz to investigate a wide range of the WM-570 band.
The maximum copolar directivity of the diagonal decreases by approximately 2 dB, while the spline-diagonal and pyramidal are less affected, as seen in Figure 4.7. Moreover, Figure 4.8 shows that the diagonal horn has a crosspolar close to half the amplitude of the copolar at $\frac{\Delta y}{\lambda} = 0.062$. The diagonal-spline's crosspolar stays below -7 dB, while the pyramidal's is significantly smaller, at values below -20 dB. The Gaussicity was calculated for each misalignment case, as shown in Figure 4.9.

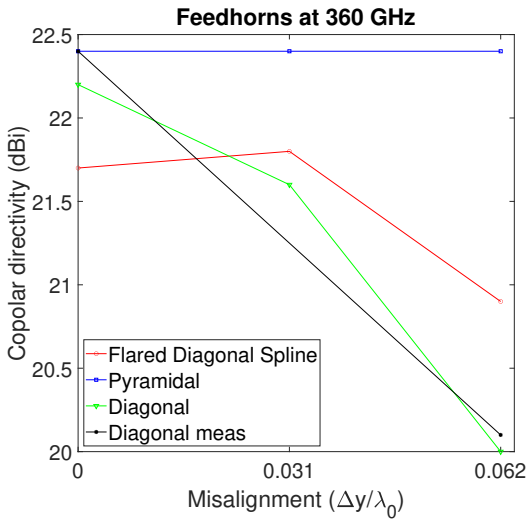

(a) Comparison at 360 GHz with the diagonal horn's measured results.

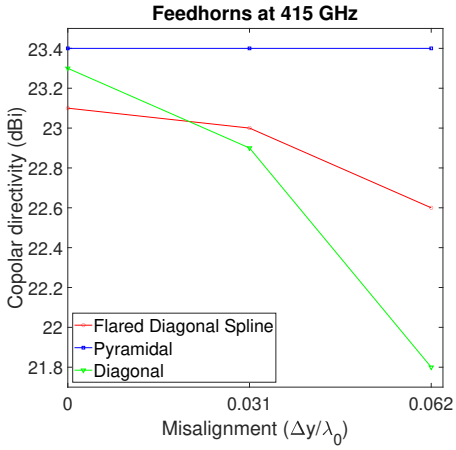

(b) Comparison at 415 GHz.

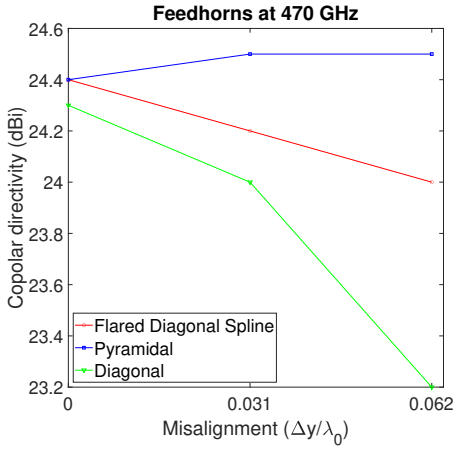

(c) Comparison at 470 GHz.

Figure 4.7: Comparison of the copolar directivity of the feedhorns at 360, 415 and 470 GHz.

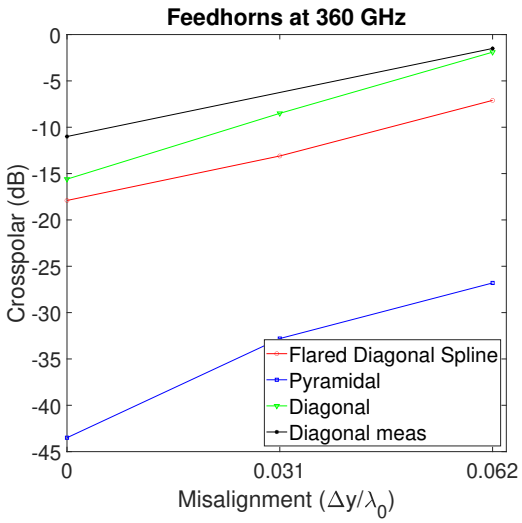

(a) Comparison at 360 GHz with the diagonal horn's measured results.

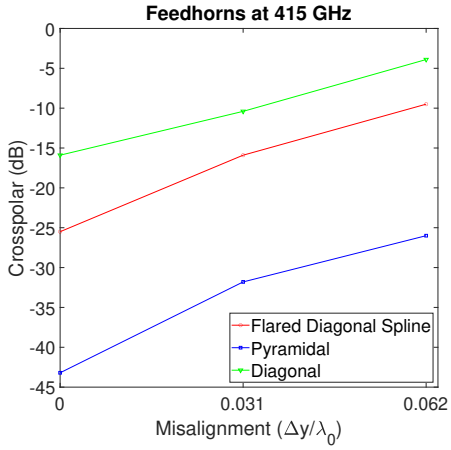

(b) Comparison at 415 GHz.

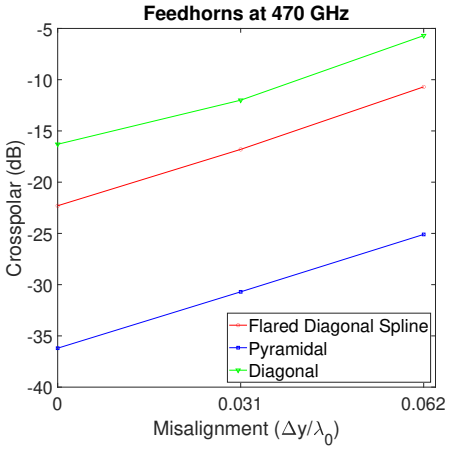

(c) Comparison at 470 GHz.

Figure 4.8: Comparison of the normalised crosspolar of the feedhorns at 360, 415 and 470 GHz.

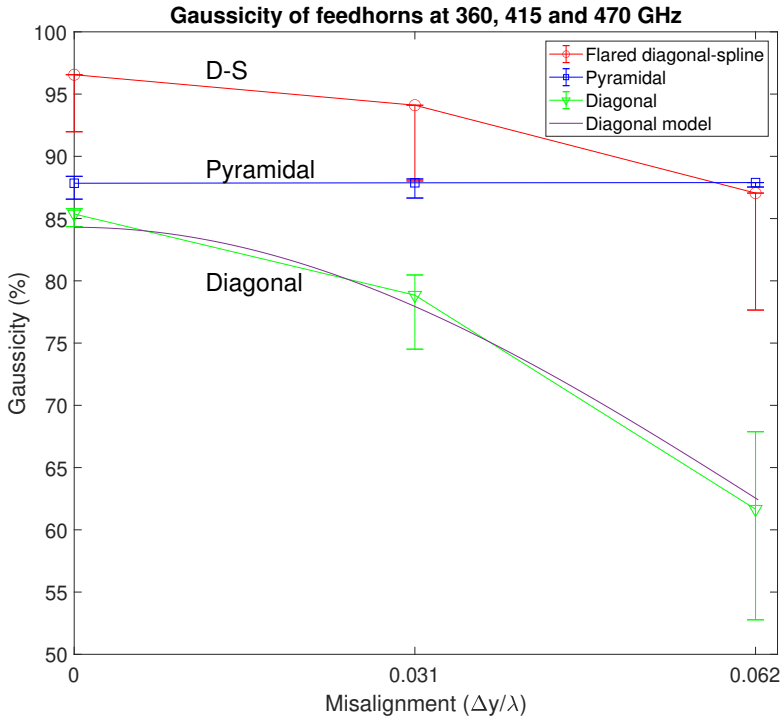

Figure 4.9: Gaussicity of the feedhorns at 360, 415 and 470 GHz in respect to split-block misalignment. The theoretical model of the standard diagonal horn at 415 GHz is included for comparison.

The simulated Gaussicity of the diagonal horn is plotted along with the theoretical model, presented in equation 3.2.10, at 415 GHz. The Gaussicity of the diagonal-spline is the highest of the three, starting at 96%. However, it also deteriorates like the diagonal horn, albeit 40% less with misalignment. The pyramidal horn stays unaffected by the misalignment due to its TE_{10} mode nature.

5

Conclusion and future work

A sensitivity analysis of split-block misalignment on the diagonal, pyramidal and diagonal-spline horn antennas is presented. The Gaussian coupling of the standard diagonal horn is sensitive to split-block misalignment due to a phase shift $\Delta\theta$ and amplitude imbalance between the two modes at the horn's aperture. The phase shift occurs due to a change in propagation factor β between the two modes, as the diagonal horn is misaligned in the E-plane. The diagonal-spline is less sensitive to the phase shift due to having a larger flare angle, resulting in a smaller $\Delta\theta$. In contrast, the pyramidal horn is robust as it only has a single mode.

The theoretical analysis is supported by full-wave electromagnetic simulations performed in a finite element method software. Moreover, a scaled experiment at 360 GHz was conducted on the standard diagonal horn to validate the analysis. By machining a block with multiple alignment options, the alignment is controlled, and its effect on the antenna is measured. A near-field measurement system was set up to obtain the far-field characteristics of the horn antenna. The copolar directivity measurement showed a 2-dB loss for a misalignment of 6% of the wavelength. This is equivalent to the loss in Gaussicity, which deteriorates from 84% to 52% at 360 GHz for the same misalignment.

Based on the electromagnetic simulations, the pyramidal horn has a coupling efficiency of 88% and is almost unaffected by the split-block misalignment. The diagonal-spline has a coupling efficiency of 96%, which deteriorates to 87% for a misalignment of 6%. This work provides insight into some drawbacks of the standard diagonal horn as a supra-terahertz E-plane split horn and proposes the pyramidal and the diagonal-spline as alternatives. Other misalignment types and fabrication errors will be studied for a more comprehensive sensitivity analysis.

Bibliography

[1] P.H. Siegel. "Terahertz technology". In: *IEEE Transactions on Microwave Theory and Techniques* 50.3 (2002), pp. 910–928. DOI: 10.1109/22.989974.

[2] G. Stacey. "THz Low Resolution Spectroscopy for Astronomy". In: *Terahertz Science and Technology, IEEE Transactions on* 1 (Oct. 2011), pp. 241–255. DOI: 10.1109/TTHZ.2011.2159649.

[3] P. H. Siegel. "THz Instruments for Space". In: *IEEE Transactions on Antennas and Propagation* 55.11 (2007), pp. 2957–2965. DOI: 10.1109/TAP.2007.908557.

[4] H.-J. Song and T. Nagatsuma. "Present and Future of Terahertz Communications". In: *IEEE Transactions on Terahertz Science and Technology* 1.1 (2011), pp. 256–263. DOI: 10.1109/TTHZ.2011.2159552.

[5] P. H. Siegel. "Terahertz Technology in Biology and Medicine". In: *IEEE Transactions on Microwave Theory and Techniques* 52.10 (2004), pp. 2438–2447. DOI: 10.1109/TMTT.2004.835916.

[6] T. G. Phillips and J. Keene. "Submillimeter Astronomy (Heterodyne Spectroscopy)". In: *Proceedings of the IEEE* 80.11 (1992), pp. 1662–1678. DOI: 10.1109/5.175248.

[7] P. F. Goldsmith. "Quasi-optical Techniques". In: *Proceedings of the IEEE* 80.11 (1992), pp. 1729–1747. DOI: 10.1109/5.175252.

[8] D.F. Filipovic, S.S. Gearhart, and G.M. Rebeiz. "Double-slot Antennas on Extended Hemispherical and Elliptical Silicon Dielectric Lenses". In: *IEEE Transactions on Microwave Theory and Techniques* 41.10 (1993), pp. 1738–1749. DOI: 10.1109/22.247919.

[9] P. Pütz et al. "Terahertz Hot Electron Bolometer Waveguide Mixers for GREAT". In: *Astronomy &amp Astrophysics* 542 (May 2012), p. L2. DOI: 10.1051/0004-6361/201218916.

[10] R. J. Wylde. "Millimetre-wave Gaussian Beam-mode Optics and Corrugated Feed Horns". In: *IEE Proceedings H: Microwaves Optics and Antennas* 131.4 (1984), pp. 258–262.

[11] H. J. Gibson et al. "A Novel Spline-Profile Diagonal Horn Suitable for Integration Into THz Split-Block Components". In: *IEEE Transactions on Terahertz Science and Technology* 7.6 (2017), pp. 657–663. DOI: 10.1109/TTHZ.2017.2752423.

[12] P. D. Potter. "Terahertz Heterodyne Receivers". In: *Microwave J.* 6 (1963), pp. 71–78.

[13] A. P. King. “The Radiation Characteristics of Conical Horn Antennas”. In: *Proceedings of the IRE* 38.3 (1950), pp. 249–251. DOI: 10.1109/JRPROC.1950.230734.

[14] J. F. Johansson and N. D. Whyborn. “The Diagonal Horn as a Sub-millimeter Wave Antenna”. In: *IEEE Transactions on Microwave Theory and Techniques* 40.5 (1992), pp. 795–800. DOI: 10.1109/22.137380.

[15] J. Oberhammer. “Overview and Recent Achievements in Silicon Micromachining for THz Systems”. In: *2019 European Microwave Conference in Central Europe (EuMCE)*. 2019, pp. 23–26.

[16] O. Glubokov et al. “Micromachined Multilayer Bandpass Filter at 270 GHz Using Dual-mode Circular Cavities”. In: *2017 IEEE MTT-S International Microwave Symposium (IMS)*. 2017, pp. 1449–1452. DOI: 10.1109/MWSYM.2017.8058894.

[17] A. Dunning, S. Srikanth, and A. R. Kerr. “A Simple Orthomode Transducer for Centimeter to Submillimeter Wavelengths”. In: *Twentieth International Symposium on Space Terahertz Technology*. Ed. by Eric Bryerton, Anthony Kerr, and Arthur Lichtenberger. Apr. 2009, pp. 191–193.

[18] A. Hammar et al. “THz Smooth-Walled Spline Horn Antennas: Design, Manufacturing and Measurements”. In: *2016 IEEE International Symposium on Antennas and Propagation (APSURSI)*. 2016, pp. 1341–1342. DOI: 10.1109/APS.2016.7696378.

[19] A. Hammar et al. “Low Noise 874 GHz Receivers for the International Submillimetre Airborne Radiometer (ISMAR)”. In: *Review of Scientific Instruments* 89 (May 2018), p. 055104. DOI: 10.1063/1.5017583.

[20] D. Jayasankar et al. “A 3.5-THz, ×6-Harmonic, Single-Ended Schottky Diode Mixer for Frequency Stabilization of Quantum-Cascade Lasers”. In: *IEEE Transactions on Terahertz Science and Technology* 11.6 (2021), pp. 684–694. DOI: 10.1109/TTHZ.2021.3115730.

[21] C. A. Balanis. *Antenna Theory: Analysis and Design*. John Wiley & Sons, 1997.

[22] H. Kogelnik and T. Li. “Laser Beams and Resonators”. In: *Proceedings of the IEEE* 54.10 (1966), pp. 1312–1329. DOI: 10.1109/PROC.1966.5119.

[23] J. F. Johansson. “A Comparison of Some Feed Types”. In: 75 (Jan. 1995), p. 82.

[24] A. W. Love. “The Diagonal Horn Antenna”. In: *Microwave J.* V (1962), pp. 117–122.

[25] A. Ludwig. “The Definition of Cross Polarization”. In: *IEEE Transactions on Antennas and Propagation* 21.1 (1973), pp. 116–119. DOI: 10.1109/TAP.1973.1140406.

[26] C. Granet et al. “A Smooth-walled Spline-profile Horn as an Alternative to the Corrugated Horn for Wide Band Millimeter-wave Applications”. In: *IEEE Transactions on Antennas and Propagation* 52.3 (2004), pp. 848–854. DOI: 10.1109/TAP.2004.825156.

[27] D. A. Montofré et al. “High-Performance Smooth-Walled Horn Antennas for THz Frequency Range: Design and Evaluation”. In: *IEEE Transactions on*

Terahertz Science and Technology 9.6 (2019), pp. 587–597. DOI: 10.1109/TTHZ.2019.2938985.

[28] R. C. Johnson, H.A. Ecker, and J.S. Hollis. "Determination of Far-field Antenna Patterns from Near-field Measurements". In: *Proceedings of the IEEE* 61.12 (1973), pp. 1668–1694. DOI: 10.1109/PROC.1973.9358.

[29] J. Stenarson et al. "Influence of Waveguide Width Errors on TRL and LRL Calibrations". In: *79th ARFTG Microwave Measurement Conference*. 2012, pp. 1–3. DOI: 10.1109/ARFTG79.2012.6291182.

[30] S. Withington and J.A. Murphy. "Analysis of Diagonal Horns Through Gaussian-Hermite Modes". In: *IEEE Transactions on Antennas and Propagation* 40.2 (1992), pp. 198–206. DOI: 10.1109/8.127404.

[31] R. Dahlback et al. "A System for THz Imaging of Low-Contrast Targets Using the Born Approximation". In: *IEEE Transactions on Terahertz Science and Technology* 2.3 (2012), pp. 361–370. DOI: 10.1109/TTHZ.2012.2189900.

[32] C. K. Wong et al. "A THz Near-field Scanning System for Antenna Measurement". In: *2017 Sixth Asia-Pacific Conference on Antennas and Propagation (APCAP)*. 2017, pp. 1–3. DOI: 10.1109/APCAP.2017.8420498.

A

Appendix 1

A.1 Extraction of Gaussicity

A.1.1 Electric field extraction

The complex electric field at the aperture is extracted from an HFSS file using the HFSS-MATLAB API made by Vijay Ramasami. See the GitHub of the API for more details on the script.

```
function HFSSApertField3(ProjectName,fldName1,fldName2,
    fldName3, ProjectPath, StartVec, StopVec, StepVec,
    close)

% HFSS Executable Path.
hfssExePath = 'C:\Program Files\AnsysEM\v231\Win64\
    ansysedt.exe';

% Script and project files.
tmpPrjFile = [pwd, '\AnyName.aedt'];
vbsfile=sprintf('%s.vbs',ProjectName);
tmpScriptFile = ['C:\...', vbsfile];

% Add paths to the required m-files.
addpath('C:\...\');
hfssIncludePaths('C:\...\');

% Create a new temporary HFSS script file.
fid = fopen(tmpScriptFile, 'wt+');
file=sprintf('%s%s.aedt',ProjectPath,ProjectName);
hfssOpenProject(fid, file,true)
hfssSetDesign(fid, 'HFSSDesign1')
hfssCreatePTS('MyGrid', StartVec, StopVec, StepVec, 'mm')
    ;
hfssEnterQty(fid, 'E', 'CmplxMag');
hfssExportToFileFC(fid, fldName1, 'MyGrid.pts', 'Setup1',
    360);
hfssEnterQty(fid, 'E', 'CmplxMag');
hfssExportToFileFC(fid, fldName2, 'MyGrid.pts', 'Setup1',
```

```
    415);
hfssEnterQty(fid, 'E', 'CmplxMag');
hfssExportToFileFC(fid, fldName3, 'MyGrid.pts', 'Setup1',
    470);
%hfssSaveProject(fid, tmpPrjFile, true);
fclose(fid);

status=hfssExecuteScript(hfssExePath, tmpScriptFile,
   false, close)

hfssRemovePaths('C:\...\');
```

A.1.2 Gaussicity calculation

The Gaussicity of the horn antenna is calculated using the extracted complex electric field.

```
%Gaussicity calculation of a horn antenna of the type
%Copol: 1 (x-copol), 2 (y-copol)
%Type: 1 (Diagonal), 2 (Conical Spline), 3 (Rectangular),
    4 (Diagonal
%spline)
%Aperture_width: aperture width (m)

function Gauss= Gauss_controller(filename,Path,Path2,x,y,
   copol,type,aperture_width)
addpath(Path);
addpath(Path2);
c=0;
if type==1
    c=0.86;
elseif type==2
    c=0.64;
elseif type==3
    c=0.35;
elseif type==4
    c=0.73;
end

A=dlmread(filename,' ', 1,0);
Ey=zeros(101,101);
Ex=zeros(101,101);
Ez=zeros(101,101);
for i=1:101
    Ey(i,:)=A(101*i-100:101*i,6);
    Ex(i,:)=A(101*i-100:101*i,5);
```

```
28      Ez(i,:)=A(101*i-100:101*i,7);
29  end
30  Ex(isnan(Ex))=0;
31  Ey(isnan(Ey))=0;
32  Ez(isnan(Ez))=0;
33
34  E=zeros(101,101,3);
35  E(:,:,1)=Ex;
36  E(:,:,2)=Ey;
37  E(:,:,3)=Ez;
38  [X,Y]=meshgrid(x,y);
39  r=sqrt(X.^2+Y.^2);
40  check=abs(X)+abs(Y);
41  omega2=c*aperture_width;
42  g=exp(-(r/omega2).^2);
43  clc
44  if copol == 1
45      test1=abs(cumtrapz(x,cumtrapz(y,E(:,:,1).*conj(g),2))
        ).^2;
46  elseif copol ==2
47      test1=abs(cumtrapz(x,cumtrapz(y,E(:,:,2).*conj(g),2))
        ).^2;
48  end
49  gauss1=test1(end)
50  test2=cumtrapz(x,cumtrapz(y,abs(E(:,:,2)).^2+abs(E(:,:,1)
    ).^2,2));
51  gauss2=test2(end)
52  test3=cumtrapz(x,cumtrapz(y,g.*conj(g),2));
53  gauss3=test3(end)
54  Gauss=100*gauss1/(gauss2*gauss3);
```

A.2 Mechanical models

The CAD mechanical model for the diagonal horn is separated into a top and a bottom block. The bottom block contains threaded holes while the top block has through holes. In addition, the top block has trenches around the waveguide and the horn to add pressure around the areas and make better contact between the split-blocks.

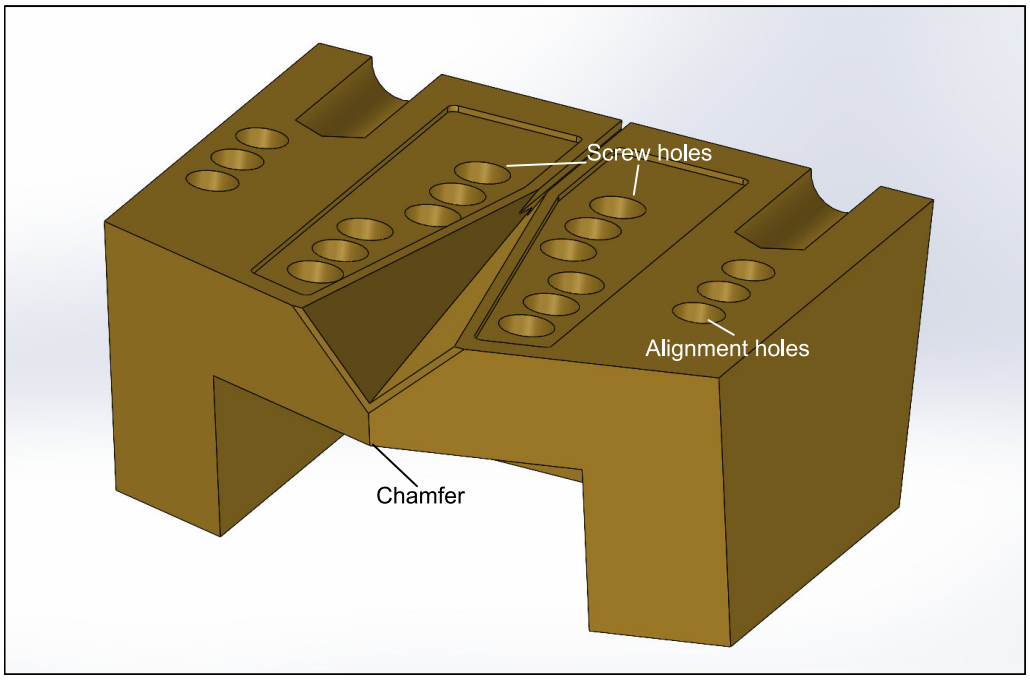

Figure A.1: CAD model of the diagonal horn's top block.

The lateral shift of the alignment holes that control the misalignment can be seen in Figure A.2.

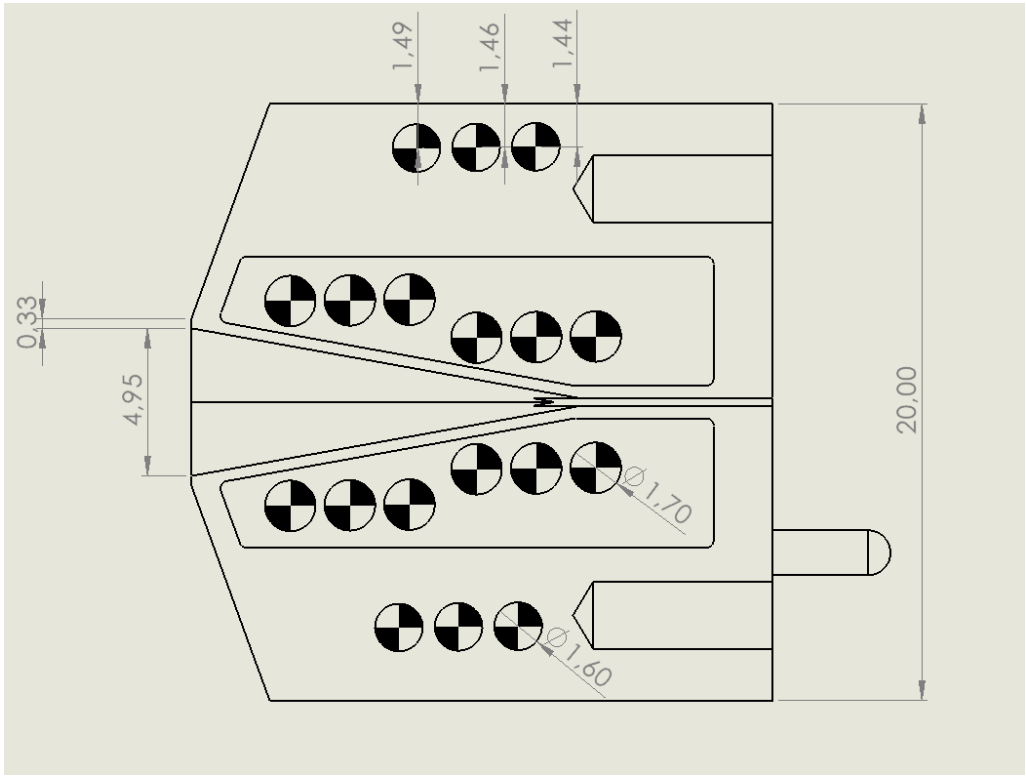

Figure A.2: Sketch of the *E-plane* split side of the block. The denoted values are in millimetres.

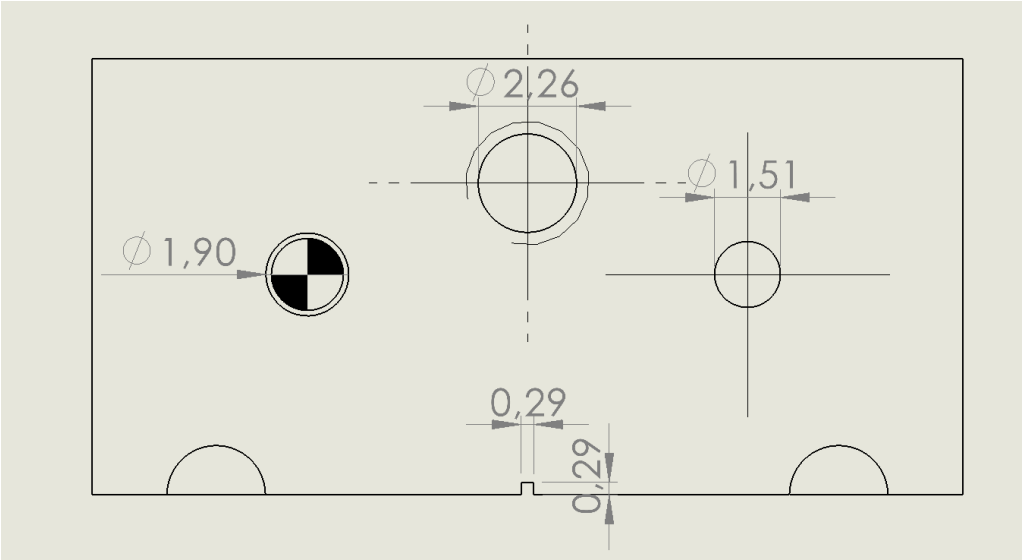

Figure A.3: Sketch of the flange side of the block. The denoted values are in millimetres.

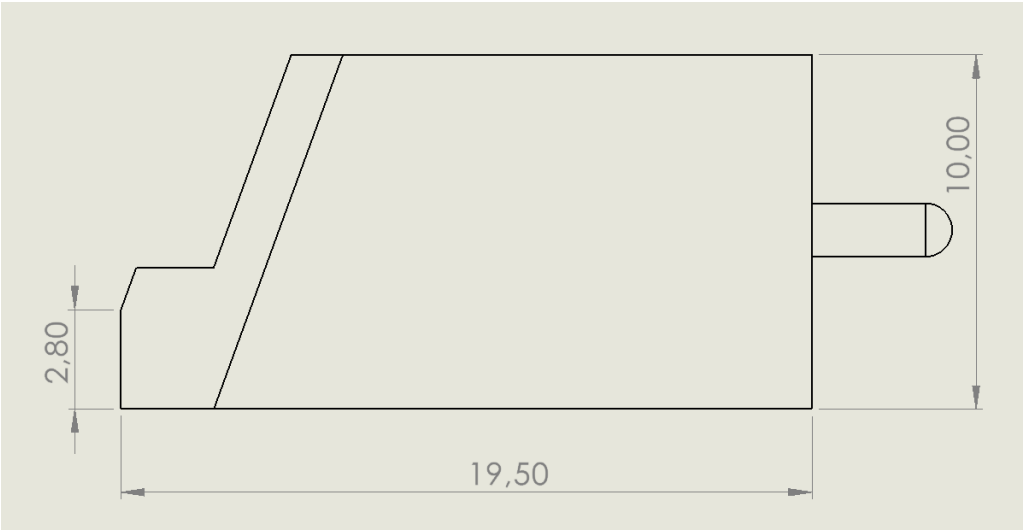

Figure A.4: Sketch of the split-block from the side. The denoted values are in millimetres.

DEPARTMENT OF SOME SUBJECT OR TECHNOLOGY
CHALMERS UNIVERSITY OF TECHNOLOGY
Gothenburg, Sweden
www.chalmers.se

CHALMERS
UNIVERSITY OF TECHNOLOGY